Global-scale distribution of ozone in the remote troposphere from ATom and HIPPO airborne field missions.

Ilann Bourgeois[1,2], Jeffrey Peischl[1,2], Chelsea R. Thompson[1,2], Kenneth C. Aikin[1,2], Teresa Campos[3], Hannah Clark[4], Róisín Commane[5], Bruce Daube[6], Glenn W. Diskin[7], James W. Elkins[8], Ru-Shan Gao[2], Audrey Gaudel[1,2], Eric J. Hintsa[1,8], Bryan J. Johnson[8], Rigel Kivi[9], Kathryn McKain[1,8], Fred L. Moore[1,8], David D. Parrish[1,2], Richard Querel[10], Eric Ray[1,2], Ricardo Sánchez[11], Colm Sweeney[7], David W. Tarasick[12], Anne M. Thompson[13], Valérie Thouret[14], Jacquelyn C. Witte[3], Steve C. Wofsy[6], and Thomas B. Ryerson[2].

[1]Cooperative Institute for Research in Environmental Sciences, University of Colorado Boulder, Boulder, CO, USA

[2]NOAA CSL, Boulder, CO, USA

[3]National Center for Atmospheric Research, Boulder, CO, USA

[4]IAGOS-AISBL, Brussels, Belgium

[5]Department of Earth and Environmental Sciences, Lamont-Doherty Earth Observatory of Columbia University, New York, NY, USA

[6]School of Engineering and Applied Sciences, Harvard University, Cambridge, MA, USA

[7]NASA Langley Research Center, Hampton, VA, USA

[8]NOAA GML, Boulder, CO, USA

[9]Finnish Meteorological Institute, Space and Earth Observation Centre, Sodankylä, Finland

[10]National Institute of Water & Atmospheric Research (NIWA), Lauder, NZ

[11]Servicio Meteorológico Nacional, Buenos Aires, Argentina

[12]Experimental Studies Research Division, MSC/Environment and Climate Change Canada, Downsview, Ontario, CA

[13]Earth Sciences Division, NASA/Goddard Space Flight Center, Greenbelt, MD, USA

[14]Laboratoire d'Aérologie, CNRS and Université Paul Sabatier, Université de Toulouse, Toulouse, FR

1 **Abstract**

2   Ozone is a key constituent of the troposphere where it drives photochemical

3 processes, impacts air quality, and acts as a climate forcer. Large-scale in situ observations of

4 ozone commensurate with the grid resolution of current Earth system models are necessary to

5 validate model outputs and satellite retrievals. In this paper, we examine measurements from

6 the Atmospheric Tomography (ATom, 4 deployments in 2016–2018) and the HIAPER Pole-

7 to-Pole Observations (HIPPO; 5 deployments in 2009–2011) experiments, two global-scale

8 airborne campaigns covering the Pacific (HIPPO and ATom) and Atlantic (ATom) basins.

9   ATom and HIPPO represent the first global-scale, vertically resolved measurements

10 of O_3 distributions throughout the troposphere, with HIPPO sampling the Pacific basin and

11 ATom sampling both the Pacific and Atlantic basins. Given the relatively limited temporal

12 resolution of these two campaigns, we first compare ATom and HIPPO ozone data to longer-

13 term observational records to establish the representativeness of our dataset. We show that

14 these two airborne campaigns captured on average 53, 54, and 38 % of the ozone variability

15 in the marine boundary layer, free troposphere, and upper troposphere/lower stratosphere

16 (UTLS), respectively, at nine well-established ozonesonde sites. Additionally, ATom

17 captured the most frequent ozone concentrations measured by regular commercial aircraft

18 flights in the northern Atlantic UTLS. We then use the repeated vertical profiles carried out

19 during these two campaigns to provide a global-scale picture of tropospheric ozone spatial

20 and vertical distributions throughout the remote troposphere. We highlight a clear

21 hemispheric gradient, with greater ozone in the northern hemisphere consistent with greater

22 precursor emissions. We also show that the ozone distribution below 8 km was similar in the

23 extra-tropics of the Atlantic and Pacific basins due to zonal circulation patterns. However,

24 twice as much ozone was found in the tropical Atlantic than in the tropical Pacific, due to

25 well-documented dynamical patterns transporting continental air masses over the Atlantic.

26 We finally show that the seasonal variability of tropospheric ozone over the Pacific and the

27 Atlantic basins is driven by transported continental plumes and photochemistry, and the

28 vertical distribution is driven by photochemistry and mixing with stratospheric air. This new

29 dataset is essential for improving our understanding of both ozone production and loss

30 processes in remote regions, as well as the influence of anthropogenic emissions on baseline

31 ozone.

1. Introduction

35 Tropospheric ozone (O_3) plays a major role in local, regional, and global air quality and

36 significantly influences Earth's radiative budget (IPCC, 2013; Shindell et al., 2012). In addition,

37 O_3 drives tropospheric photochemical processes by controlling hydroxyl radical (OH)

38 abundance, which subsequently controls the lifetime of other pollutants including volatile

39 organic compounds (VOCs), greenhouse gases, and some stratospheric ozone-depleting

40 substances (Crutzen, 1974; Levy, 1971). Sources of O_3 to the troposphere include downward

41 transport from the stratosphere (Junge, 1962) and photochemical production from precursors

42 such as carbon monoxide (CO), methane (CH_4), and VOCs in the presence of nitrogen oxides

43 (NO_x) emitted by natural or anthropogenic sources (Monks et al., 2009). Tropospheric O_3 sinks

44 include photo-dissociation, chemical reactions, and dry deposition. Owing to its relatively long

45 lifetime (~23 days in the troposphere; Young et al., 2013), O_3 can be transported across intra-

46 hemispheric scales. O_3 mixing ratios over a region thus depend not only on local and regional

47 sources and sinks, but also on long-range transport. Further, the uneven density of O_3 monitoring

48 locations around the globe leads to significant sampling gaps, especially near developing nations

49 (Gaudel et al., 2018). The troposphere over the remote oceans is among the least-sampled

50 regions, despite hosting 60–70 % of global tropospheric O_3 burden (Holmes et al., 2013). Since

51 the early 1980's, several aircraft campaigns have periodically addressed this paucity of remote

52 observations, most notably under the umbrella of the Global Tropospheric Experiment (GTE), a

53 major component of the National Aeronautics and Space Administration (NASA) Tropospheric

54 Chemistry Program (https://eosweb.larc.nasa.gov/project/gte/gte_table).

55   Continuing this tradition, the Atmospheric Tomography mission (ATom,

56 https://espo.nasa.gov/atom) was a NASA Earth Venture airborne field project to address the

57 sparseness of atmospheric observations over remote ocean regions by systematically sampling

58 the troposphere over the Pacific and Atlantic basins along a global-scale circuit (Fig. 1). ATom

59 deployed an extensive payload on the NASA DC-8 aircraft, measuring a wide range of chemical,

60 microphysical, and meteorological parameters in repeated vertical profiles from 0.2 km to over

61 13 km altitude, from the Arctic to the Antarctic over the Pacific and Atlantic Oceans, in four

62 separate seasons from 2016 to 2018. One of the main goals of ATom was to develop an

63 observation-based climatology of the composition of the remote atmosphere using airborne in

64 situ measurements from global-scale sampling flights.

65   ATom built on a previous study, the HIAPER Pole-to-Pole Observations mission

66 (HIPPO, https://www.eol.ucar.edu/field_projects/hippo). The goal of HIPPO was to measure

67 atmospheric distributions of important greenhouse gases and reactive species over the Pacific

68 Ocean, from the surface to the tropopause, five times during different seasons from 2009 to

69 2011. Together, ATom and HIPPO provide unique information about the altitudinal and

70 latitudinal composition of the remote troposphere over the Pacific, and over the Atlantic for

71 ATom.

72   Here we use existing ozonesonde and commercial aircraft observations of O_3 at selected

73 locations along the ATom and HIPPO circuits to provide a climatological context for the

74 altitudinal, latitudinal, and seasonal distributions of O_3 derived from the systematic airborne in

75 situ "snapshots". Long-term O_3 observations are obtained from decades of ozonesonde vertical

76 profiles (e.g., Oltmans et al., 2013; Thompson et al., 2017) and from ~60,000 flights using the

77 In-service Aircraft for a Global Observing System (IAGOS) infrastructure (Petzold et al., 2015;

78 http://www.iagos.org). Ozonesondes have typically been launched weekly for two decades or

79 more, depending on the site, and have sampled a wide range of air masses across the globe, from

80 O_3-poor remote surface locations to the O_3-rich stratosphere. IAGOS commercial aircraft have

81 provided daily measurements in the upper troposphere and lower stratosphere (UTLS) for the

82 past 25 years, especially over the northern midlatitudes between America and Europe.

83 Combined, the ozonesonde and IAGOS datasets offer robust measurement-based climatologies

84 that quantify the full expected range of atmospheric O_3 variability with altitude and season.

85   The in-situ data from temporally-limited intensive field studies can be placed in context

86 by comparing them with long-term ozonesonde and commercial aircraft monitoring data. We

87 show that ATom and HIPPO measurements capture the spatial and, in some cases, the temporal

88 dependence of O_3 in the remote atmosphere. Then, we use the geographically extensive ATom

89 and HIPPO vertical profile data to establish a more complete measurement-based benchmark for

90 O_3 abundance and distribution in the remote marine atmosphere.

91

92   **2. Measurements**

93 2.1 ATom

94   The four ATom circuits occurred in July–August 2016 (ATom-1), January–February

95 2017 (ATom-2), September–October 2017 (ATom-3), and April–May 2018 (ATom-4), thus

96   spanning all four seasons in both hemispheres over a two-year timeframe (Table S1). The

97   mission in total consisted of 48 science flights and 548 vertical profiles distributed nearly equally

98   along the global circuit. All four deployments completed roughly the same loop, starting and

99   ending in Palmdale, California, USA (Fig. 1). A notable addition during ATom-3 and -4 were

100   out-and-back flights from Punta Arenas, Chile to sample the Antarctic troposphere and UTLS.

101   O_3 was measured using the National Oceanic and Atmospheric Administration (NOAA)

102   nitrogen oxides and ozone (NO_yO_3) instrument. The O_3 channel of the NO_yO_3 instrument is

103   based on the gas-phase chemiluminescence (CL) detection of ambient O_3 with pure NO added as

104   a reagent gas (Ridley et al., 1992; Stedman et al., 1972). Ambient air is continuously sampled

105   from a pressure-building ducted aircraft inlet into the NO_yO_3 instrument at a typical flow rate of

106   1025.0 ± 0.2 standard cubic centimeters per minute (sccm) in flight. Pure NO reagent gas flow

107   delivered at 3.450 ± 0.006 sccm is mixed with sampled air in a pressure (8.00 ± 0.08 Torr) and

108   temperature (24.96 ± 0.01 °C) controlled reaction vessel. NO-induced CL is detected with a dry-

109   ice-cooled, red-sensitive photomultiplier tube and the amplified digitized signal recorded using

110   an 80 MHz counter; pulse coincidence corrections at high count rates were applied, but are

111   negligible for the data presented in this work. The instrument sensitivity for measuring O_3 under

112   these conditions is 3150 ± 80 counts per second per part per billion by volume (ppbv) averaged

113   over the entire ATom circuit. CL detector calibrations were routinely performed both on the

114   ground and during flight by standard addition of O_3 produced by irradiating ultrapure air with

115   185 nm UV light and independently measured using UV optical absorption at 254 nm. All O_3

116   measurements were taken at a temporal resolution of 10 Hz, averaged to 1 Hz, and corrected for

117   the dependence of instrument sensitivity on ambient water vapor content (Ridley et al., 1992).

118   Under these conditions the total estimated 1 Hz uncertainty at sea level is $\pm$ (0.015 ppbv + 2 %).

119   A commercial dual-beam photometer (2B Technologies model 211) based on UV optical

120   absorption at 254 nm also measured O_3 on ATom, with an estimated uncertainty of $\pm$ (1.5 ppbv +

121   1 %) at a 2-second sampling resolution. Comparison of the 2B absorption instrument O_3 data to

122   the NO_yO_3 CL instrument O_3 data agreed to within combined instrumental uncertainties, lending

123   additional confidence to the NO_yO_3 CL instrument calibration. For the ATom project we use

124   NO_yO_3 instrument O_3 data in the following analyses.

125   Data from two CO measurements were combined in this analysis. The Harvard quantum

126   cascade laser spectrometer (QCLS) instrument used a pulsed quantum cascade laser tuned at

127   ~2160 cm⁻¹ to measure the absorption of CO through an astigmatic multi-pass sample cell with

128   76 m path length and detection using a liquid-nitrogen-cooled HgCdTe detector (Santoni et al.,

129   2014). In-flight calibrations were conducted with gases traceable to the NOAA World

130   Meteorological Organization (WMO) X2014A scale, and the QCLS observations have an

131   accuracy and precision of 3.5 and 0.15 ppb for 1 Hz data, respectively. CO was also measured by

132   the NOAA cavity ring-down spectrometer (CRDS, Picarro, Inc., model G2401-m) in the 1.57

133   μm region with a total uncertainty of 5.0 ppbv for 1 Hz data (Karion et al., 2013). The NOAA

134   Picarro was also calibrated to the NOAA CO-X2014A scale. The combined CO data (CO-X)

135   used here corresponds to the QCLS data, with the Picarro measurement used to fill calibration

136   gaps in the QCLS time series.

137   Water (H_2O) vapor was measured using the NASA Langley Diode Laser Hygrometer

138   (DLH), an open-path infrared absorption spectrometer that uses a laser locked to a water vapor

139   absorption feature at ~1.395 μm. Raw data are processed at the instrument's native ~100 Hz

140   acquisition rate and averaged to 1 Hz with an overall measurement accuracy within 5 %.

141

142   2.2 HIPPO

143   The HIPPO mission consisted of five seasonal deployments over the Pacific basin

144   between 2009 and 2011, from the North Pole to the coastal waters of Antarctica (Wofsy, 2011).

145   HIPPO deployments consisted of two transects, southbound and northbound, and occurred in

146   January 2009 (HIPPO-1), October–November 2009 (HIPPO-2), March–April 2010 (HIPPO-3),

147   June–July 2011 (HIPPO-4) and August–September 2011 (HIPPO-5). The platform used was the

148   NSF Gulfstream V (GV) aircraft. More details can be found in Table S1.

149   A NOAA custom-built dual-beam photometer based on UV optical absorption at 254 nm

150   was used to measure O_3 (Proffitt and McLaughlin, 1983). The uncertainty of the 1 Hz O_3 data is

151   estimated to be ± (1 ppbv + 5 %) for 1 Hz data. A commercial dual-beam O_3 photometer (2B

152   Technologies model 205) based on UV optical absorption at 254 nm was also included in the

153   HIPPO payload. Comparison of the 2B O_3 data to the NOAA O_3 data showed general agreement

154   within combined instrument uncertainties on level flight legs. For the HIPPO project we use

155   NOAA O_3 data in the following analyses.

156   Data from two CO measurements were combined in this analysis. The QCLS instrument

157   was the same instrument as used during ATom and described in section 2.1. CO was also

158   measured by an Aero-Laser AL5002 instrument using vacuum UV resonance fluorescence (in

159   the 170–200 nm range) instrument with an uncertainty of $\pm$ (2 ppbv + 3 %) at a 2-second

160   sampling resolution. The combined CO data (CO-X) used here corresponds to the QCLS data,

161   with the Aero-Laser measurement used to fill calibration gaps in the QCLS time series.

162

163   2.3 IAGOS

164   IAGOS is a European Research Infrastructure that provides airborne in situ chemical,

165   aerosol, and meteorological measurements using commercial aircraft (Petzold et al., 2015). The

166   IAGOS Research Infrastructure includes data from both the CARIBIC (Civil Aircraft for the

167   Regular Investigation of the atmosphere Based on an Instrument Container; Brenninkmeijer et

168   al., 2007) and MOZAIC (Measurements of OZone and water vapor by Airbus In-service

169   airCraft; Marenco et al., 1998) programs, providing measurements from ~60,000 flights since

170   1994. We note the relative lack of IAGOS data over the Pacific compared to the Atlantic (shorter

171   temporal record, lower flight frequency, and much fewer flights with concomitant O_3 and CO

172   measurements), and therefore limited the comparison to the Atlantic. Because commercial

173   aircraft cruise altitudes over the ocean are predominantly between 9 and 12 km, the comparison

174   between ATom and IAGOS is further limited to the UTLS (Fig. 1). More details are shown in

175   Table S1.

176   Identical dual-beam UV absorption photometers measured O_3 aboard the IAGOS flights.

177   An instrument comparison demonstrated that the photometers (standard model 49, Thermo

178   Scientific, modified for aircraft use) showed good consistency in measuring O_3 following an

179   inter-comparison experiment (Nédélec et al., 2015). The associated uncertainty is $\pm$ (2 ppbv + 2

180   %) at a 4-second sampling resolution (Thouret et al., 1998).

181   CO measurements were made using infra-red absorption photometers (standard model 48

182   Trace Level, Thermo Scientific, modified for aircraft use) with an uncertainty of $\pm$ (5 ppbv + 5

183   %) at a 30-second sampling resolution (Nédélec et al., 2003, 2015).

184

185   2.4 Ozonesondes

186   Ozonesondes have measured the vertical distribution of O_3 in the atmosphere for decades,

187   and provide some of the longest tropospheric records that are commonly used to determine

188   regional O_3 trends (Gaudel et al., 2018; Leonard et al., 2017; Oltmans et al., 2001; Tarasick et

189   al., 2019a; Thompson et al., 2017). Ozonesonde launching sites are operated by the NOAA

190   ESRL Global Monitoring Division (GMD), NASA Goddard's Southern Hemisphere Additional

191   OZonesondes (SHADOZ) program, the New Zealand National Institute of Water & Atmospheric

192   Research (NIWA), the National Meteorological Center of Argentina (SNMA) in collaboration

193   with the Finnish Meteorological Institute (FMI), or Environment and Climate Change Canada. A

194   more detailed description of each ozonesonde site and corresponding dataset can be found in

195   Tables S1 and S2. All sites use electrochemical concentration cell (ECC) ozonesondes that rely

196   on the potassium iodide electrochemical detection of O_3, and which provide a vertical resolution

197   of about 100 m (Komhyr, 1969). The associated uncertainty is usually ± (5–10 %) (Tarasick et

198   al., 2019a; Thompson et al., 2019; Witte et al., 2018).

199

200   2.5 Data analysis

201   In this analysis, ATom flight tracks were divided into the Atlantic and Pacific basins, and

202   further subdivided into five regions within those basins: tropics, and northern and southern

203   middle- and high-latitudes. Vertical profiles presented graphically in this paper show O_3 median

204   values and the 25th to 75th percentile range within the 0–12 km tropospheric column sampled by

205   the DC-8 aircraft. These medians were obtained by averaging with equal weight the individual

206   profiles within each region over 1 km altitude bins.

207   HIPPO flight tracks are illustrated in Figure 1. The flight segments used for comparison

208   with ATom were binned into the same Pacific latitude and longitude bands as for ATom. HIPPO

209   vertical profile data are derived using the same methodology as for ATom.

210   All IAGOS flight tracks over the northern and tropical Atlantic are represented in Figure

211   1 in green. The latitude bands used to parse IAGOS data are consistent with the ones used for

212   ATom. The longitude bands are 50° W to 20° W in the tropics, 50° W to 10° W in the northern

213   midlatitudes, and 110° W to 10° W in the northern high-latitudes. Variations of the longitude

214   band widths do not significantly affect the O_3 distributions measured by IAGOS. Data from all

215   flights from 1994 to 2017 were included in the IAGOS dataset considered here, and were then

216   divided into two altitude bins (8–10 km and 10–12 km) in order to better understand the

217   influence of different O_3 sources (e.g., anthropogenic, stratospheric) on these two layers of the

218   atmosphere.

219   We compare the ozonesonde measurements to ATom and HIPPO aircraft data sampled

220   within 500 km of each ozonesonde launching site, since we expect a robust correlation in the free

221   troposphere within this distance (Liu et al., 2009). We used the surface coordinates of the

222   ozonesonde sites because the in-flight coordinates of ozonesondes are not available at all sites.

223   For comparison with ozonesonde long term records, we consider three regions of the

224   atmosphere: boundary layer (0–2 km), free troposphere (2–8 km), and UTLS (8–12 km). For

225   each layer, we compared monthly O_3 distributions from ozonesondes with the corresponding

226   seasonal O_3 distributions from aircraft measurements using the skill score (S_{score}) metric (Perkins

227   et al., 2007). The S_{score} is calculated by summing the minimum probability of two normalized

228   distributions at each bin center, and therefore measures the overlapping area between two

229   probability distribution functions. If the distributions are identical, the skill score will equal 100

230   % (see Fig. S1 for further examples). Note the S_{score} is positively correlated with the size of the

231   bin used to compare distributions. Here we chose a bin size of 5 ppbv, which is larger than the

232   combined precision of ATom, HIPPO, and IAGOS measurements, but small enough to separate

233   distinct air masses and their influence on O_3 distribution. Variables such as the distance to each

234   ozonesonde launching site (500 km in this study), the bin size of the O_3 distributions (5 ppbv in

235   this study), and the length of each ozonesonde record (full length in this study) can shift the

236   vertically-averaged S_{score} value by up to 8 % (Table S3). We therefore treat this 8 % as a rough

237   estimate of the precision of the S_{score} values presented here.

238   All three techniques (chemiluminescence, UV absorption, and ECC) used to measure O_3

239   for the datasets analyzed in this work have been shown to provide directly-comparable accurate

240   measurements with well-defined uncertainties (Tarasick et al., 2019a).

241

242   2.6 Back trajectory analysis

243   Analysis of back trajectories for air masses sampled during airborne missions is useful to

244   examine the air mass source regions and causes for O_3 variability over the Pacific and Atlantic

245   Oceans. We calculated ten-day back trajectories using the Traj3D model (Bowman, 1993;

246   Bowman and Carrie, 2002) and National Centers for Environmental Prediction (NCEP) global

247   forecast system (GFS) meteorology. Trajectories were initialized each minute along all of the

248   ATom flight tracks.

249

250 **3. Comparison of ATom and HIPPO O_3 distributions to longer-term observational**

251 **records**

252   Here we use existing ozonesonde and IAGOS observations of O_3 at selected locations

253 along the ATom and HIPPO circuits to provide a climatological context for O_3 distributions

254 derived from the systematic airborne in situ "snapshots". We quantify how much of O_3

255 variability, occurring on timescales ranging from hours to decades, was captured by the

256 temporally-limited HIPPO and ATom missions.

257

258 3.1. Comparison to ozonesondes

259   ATom and HIPPO explored the fidelity with which airborne missions represent O_3

260 climatology in the remote troposphere. Here, we show that aircraft-measured median O_3 follows

261 the seasonal ozonesonde-measured median O_3 cycle at most of the sites studied here, and at

262 almost all altitudes – with a few exceptions (Figs. 2 and 3). Figure 2 plots the monthly median O_3

263 measurements from the tropical ozonesonde sites in three altitude bins, along with the median

264 values obtained from HIPPO and ATom measurements. Figure 3 plots the same for the

265 extratropical sites. Figure 4 correlates the median O_3 measured by aircraft in Figures 2 and 3

266 with those measured by ozonesondes. At the Eureka site, the winter and spring ATom

267 deployments recorded a significantly lower median O_3 compared to the corresponding

268 ozonesonde monthly median O_3 in the 0–2 km range (Fig. 3). Eureka is frequently subject to

269 springtime O_3 depletion events at the surface due to atmospheric bromine chemistry, which is

270 well recorded by the ozonesonde record (Fig. 3; Tarasick and Bottenheim, 2002). Sampling

271 during O_3 depletion events significantly lowered the ATom winter and springtime O_3

272 distributions near this site. In the 2–8 km range, there is a very good seasonal agreement between

273 ATom/HIPPO and the ozonesondes (Fig. 4b). Most seasonal differences are found above 8 km

274 (e.g., ATom in February at Trinidad Head and in May at Eureka; Fig. 3) and can be linked to the

275 occurrence – or absence – of stratospheric air sampling during ATom and HIPPO. However, it is

276 straightforward to remove stratospheric airmasses from airborne data using filters based on

277 meteorology (potential vorticity) or composition (H_2O/O_3) (e.g., Cohen et al., 2018). In the

278 absence of stratospheric air mixing (< 8 km in Fig. 4), ATom/HIPPO successfully capture a large

279 fraction of O_3 climatology everywhere (Figs. 4b and 4c).

280

281   Figures 5 and 6 show vertical profiles of O_3 distributions by season at each ozonesonde

282   site, along with comparisons to HIPPO and ATom vertical profiles. Our analysis reveals that O_3

283   distributions derived from the ATom and HIPPO seasonal "snapshots" capture 30–71 % of the 1

284   km-vertically binned O_3 distribution established by long-term ozonesonde climatologies. For the

285   nine ozonesonde sites considered here, ATom and HIPPO captured on average 53 %, 54 %, and

286   38 % of the O_3 distribution in the 0–2 km, 2–8 km, and 8–12 km altitude bins, respectively.

287   Larger differences between ATom/HIPPO and the ozonesonde records in the UTLS (8–

288   12 km) can be ascribed to O_3 variability from stratospheric–tropospheric exchanges, which are

289   not always captured by the ATom and HIPPO missions. This increased O_3 variability in the

290   UTLS is well-described by the long term ozonesonde records at Lauder, Trinidad Head, Eureka,

291   Ushuaia, and Marambio (Figs. 3 and 6). In these middle- and high-latitude locations in both

292   hemispheres, O_3 variability is especially pronounced during winter and spring, time periods

293   favorable to more frequent stratospheric air mixing (Greenslade et al., 2017; Lin et al., 2015;

294   Tarasick et al., 2019b). Furthermore, the probability of sampling stratospheric air masses at

295   ATom and HIPPO ceiling altitude (12–14 km) increases with latitude, resulting in a lower S_{score}

296   between the ATom/HIPPO and ozonesonde datasets at the extra-tropical sites than at the tropical

297   sites (Figs. S2a and S2b).

298   In the boundary layer (0–2 km) of the remote troposphere, O_3 variability is predominantly

299   impacted by loss mechanisms. Ozonesonde records show instances of O_3 mixing ratios lower

300   than 10 ppbv throughout the year in the boundary layer at the nine sites studied here (Figs. 2 and

301   3). The lowest O_3 mixing ratios are a result of (a) photochemical destruction over the oceans in

302   the tropics (Monks et al., 1998, 2000; Thompson et al., 1993), (b) O_3-destroying halogen

303   emissions in polar regions in springtime (e.g., Fan and Jacob, 1992), and (c) transport of O_3-poor

304   oceanic air over the midlatitude sites (e.g., Neuman et al., 2012).

305   ATom and HIPPO best describe the O_3 distribution in the free troposphere (2–8 km; Figs.

306   S2a and S2b). This suggests that airborne campaigns can capture global baseline O_3 values,

307   along with the long-range transport of O_3 pollution plumes often lofted to this altitude range and

308   responsible for O_3 variability.

309

310   While ATom consisted of one transect per ocean per season, HIPPO covered the Pacific

311   twice per seasonal deployment (southbound and northbound). The 1 km-binned S_{score} is on

312   average higher when two combined seasonal HIPPO flights (southbound and northbound) were

313   available to compare to ozonesonde records, as opposed to when comparing O_3 profiles from

314   individual HIPPO transects with ozonesonde records (Fig. S2c). In addition, two seasonal flights

315   during HIPPO reduced the occurrence of low S_{score} values. This S_{score} decrease from flying only

316   one Pacific transect only during ATom was traded for the increase of vertical profiles over the

317   Atlantic Basin, which were not sampled during HIPPO. Future airborne missions with multiple

318   seasonal vertical profiles over large-scale regions would be ideal to better depict the full range of

319   tropospheric O_3 variability.

320

321   3.2. Comparison to IAGOS

322   IAGOS O_3 and CO observations in the northern Atlantic UTLS provide a measurement-

323   based climatology at commercial aircraft cruise altitudes for comparison to ATom. Simultaneous

324   measurements of O_3 and CO are of particular interest because CO provides a long-lived tracer of

325   continental emissions, which helps to differentiate O_3 sources (Cohen et al., 2018). We note that

326   while IAGOS measurements encompass hundreds of seasonal flights (depending on the region),

327   ATom sampled within each latitude band and season on one or two flights only (Fig. 1). Thus,

328   variability in the UT that occurred on timescales longer than a day were not captured by ATom.

329   Consequently, it is not surprising to see that ATom systematically under-sampled tropospheric

330   O_3 (and CO) variability compared to IAGOS at all latitudes in the northern Atlantic (Figs. 7 and

331   8). ATom captured on average 40 % of the O_3 variability measured by IAGOS in the Atlantic

332   UTLS (Fig. 7), on par with the S_{score} of 38 % obtained when comparing ATom and HIPPO to

333   ozonesonde data (see section 3.1).

334

335   In the middle- and high-latitudes, the shapes of the O_3 vs. CO scatterplots from IAGOS

336   data demonstrate that distinct sources contribute to O_3 levels in the UTLS (Figs. 8a and 8b;

337   Gaudel et al., 2015). The high O_3 (>150 ppbv) – low CO (<100 ppbv) range corresponds to

338   intrusions of stratospheric air, which were mostly sampled in the spring season during ATom,

339   supporting previous observations of increased stratospheric air mixing during this season (Lin et

340   al., 2015; Tarasick et al., 2019b). The low O_3 (<50 ppbv) – low CO (<100 ppbv) range

341   corresponds to the tropospheric baseline air, whereas the intermediate O_3 (50–120 ppbv) – high

342   CO (>100 ppbv) range generally represents the influence of air masses transported from

343   continental regions. During ATom, high O_3 and low CO in the middle- and high-latitude UTLS

344   were typical of stratospheric and baseline tropospheric air mixing.

345

346   O_3 measured during IAGOS rarely exceeds 150 ppbv in the northern tropical Atlantic

347   UTLS (Fig. 8c). This is expected because the tropical tropopause is typically situated between 13

348   and 17 km altitude and IAGOS flights typically cruise below 12 km. Therefore, instances of

349   stratospheric intrusions at IAGOS flight altitudes are limited. O_3 measured during ATom in the

350   tropical Atlantic above 8 km was generally positively correlated with CO, showing the

351   contribution of tropospheric O_3 production from continental sources reaching high altitudes.

352   Given this variability, the ATom data do not capture the extrema of UTLS O_3 variability in the

353   IAGOS measurements (Figs. 7 and 8). However, the most frequently measured O_3 and CO

354   values from ATom overlap with the most frequently measured O_3 and CO values from IAGOS

355   (contours in Fig. 8), suggesting that ATom captured the mode of the O_3 and CO distributions

356   from IAGOS in the northern Atlantic UTLS.

357

358   **4. O_3 distributions in the remote troposphere from ATom and HIPPO**

359   We have established the fidelity of ATom and HIPPO O_3 data by comparison to

360   measurement-based climatologies of tropospheric O_3 from well-established ozonesonde and

361   commercial aircraft monitoring programs. In the following sections we exploit the systematic

362   nature of the ATom and HIPPO vertical profiles to provide a global-scale picture of tropospheric

363   O_3 distributions in the remote atmosphere. Figure 9 presents the altitudinal, latitudinal, and

364   seasonal distribution of tropospheric O_3 during ATom and HIPPO. Higher O_3 was measured

365   during ATom & HIPPO in the Northern Hemisphere (NH) than in the Southern Hemisphere

366   (SH), both in the Pacific and in the Atlantic. This holds true throughout the tropospheric column

367   from 0 to 8 km, both in the middle- and high-latitudes (Fig. S3). In the midlatitudes below 8 km,

368   median O_3 ranged between 25 and 45 ppbv in the SH, and between 35 and 65 ppbv in the NH. In

369   the high latitudes below 8 km, median O_3 ranged between 30 and 45 ppbv in the SH, and

370   between 40 and 75 ppbv in the NH. Notable features in the global O_3 distribution are discussed

371   in more detail in the following sections. Figure 10 presents the vertically-resolved distribution of

372   tropospheric O_3 from 0–12 km for the Atlantic (ATom in green) and for the pacific (ATom in

373   pink, HIPPO in blue). S_{score} values resulting from the comparison of HIPPO and ATom Pacific

374 distributions are shown with blue diamonds, and from the comparison of ATom Atlantic and

375 Pacific distributions with pink squares. Figure 11 is derived from Figure 10 and gives the S_{score}

376 values against altitude in the first panel, as well as the relative difference of median O_3 from 0 to

377 8 km in the second panel. Figure

378

379   4.1. Tropics

380   **Vertical distribution.** O_3 is at a minimum in the tropical marine boundary layer (MBL),

381 especially over the Pacific (Fig. 10a). The lowest measured O_3 in this region was 5.4 ppbv in

382 May during ATom, and 3.5 ppbv in January during HIPPO. The tropical MBL is a net O_3 sink

383 owing to very slow O_3 production rates – NO levels averaged 22 ± 12 pptv in the Pacific and

384 Atlantic MBL during ATom – and rapid photochemical destruction rates of O_3 in a sunny, humid

385 environment (Kley et al., 1996; Parrish et al., 2016; Thompson et al., 1993). Deep stratospheric

386 intrusions into the Pacific MBL were not observed in ATom or HIPPO, in contrast to reports

387 from previous studies (e.g., Cooper et al., 2005; Nath et al., 2016). In the tropics, marine

388 convection within the intertropical convergence zone (ITCZ) is associated with relatively low O_3

389 values throughout the tropospheric column, with median O_3 mixing ratios less than 25 ppbv

390 below 4 km altitude in the tropical Pacific (Fig. 10a; Oltmans et al., 2001). The relative

391 difference between ATom Atlantic and Pacific median O_3 in the tropics below 8 km is

392 consistently higher than a factor of 1.5, with an average S_{score} of 43 % (Figs. 10a and 11b). We

393 ascribe this difference to O_3 production from biomass burning (BB) emissions in the continental

394 regions surrounding the tropical Atlantic; back trajectories from the ATom flight tracks show the

395 tropical Atlantic is strongly affected by transport from BB source regions in both Africa and

396 South America (Fig. S4; Jensen et al., 2012; Sauvage et al., 2006; Stauffer et al., 2018;

397 Thompson et al., 2000). Although ATom and HIPPO data show evidence for extensive and

398 widespread BB influence on O_3 in the Pacific as well, O_3 mixing ratios are consistently more

399 elevated throughout the tropospheric column in the Atlantic. One reason is closer proximity of

400 the mid-ocean Atlantic flight tracks to O_3 precursor source regions. In addition, the positive

401 correlation of O_3 enhancements with black carbon (Katich et al., 2018) and reactive nitrogen

402 species (Thompson et al., personal communication) indicate BB influence. These findings

403 confirm studies that previously highlighted the impact of African BB emissions on O_3 production

404 in the tropical Atlantic (e.g., Andreae et al., 1994; Fishman et al., 1996; Jourdain et al., 2007;

405   Williams et al., 2010). Lightning NO_x also play a role in the buildup of O_3 over the tropical

406   Atlantic at certain times of year (Moxim and Levy, 2000; Pickering et al., 1996).

407   **Seasonality.** The seasonal variation of vertical profiles of O_3 in the tropics is lower

408   throughout the column compared to the extra-tropics (Fig. 12), in part due to less stratospheric

409   influence at the highest tropical altitudes. The remoteness of the tropical Pacific flight paths from

410   continental pollution sources also drives the lower seasonal variability here compared to the

411   tropical Atlantic, where BB influence peaks in June–August and October–November,

412   characterized by high O_3 (> 75 ppbv) and high CO (>100 ppbv) (Fig. 13f), significantly increases

413   the O_3 vertical distribution compared to the other seasons (Figs. 12c, 12h, and 12m). Finally,

414   photochemistry, which regulates O_3 net balance in the troposphere, is less seasonally variable in

415   the tropics than in the extra-tropics, where the photolysis frequency of O_3 (j(O_3)) and

416   photochemical production of O_3 fluctuate annually with solar zenith angle.

417   **O_3 minima and maxima.** Coincident O_3 and CO enhancements were observed in the

418   tropical Atlantic for each ATom circuit (Figs. 9 and 13f), suggesting a year-round influence of

419   continental emissions and distinctive dynamics in this region (Krishnamurti et al., 1996;

420   Thompson et al., 1996). In the tropical Pacific, the April–May period stands out due to an O_3 and

421   CO enhancement episode during HIPPO (Fig. 9) that was attributed to the transport of

422   anthropogenic and BB emissions from southeast Asia (Shen et al., 2014).

423   Deep convection in the tropics brings O_3-poor (<15 ppbv) air to the upper troposphere (Kley et

424   al., 1996; Pan et al., 2015; Solomon et al., 2005). However, the spatial extent of these events

425   remains poorly constrained. Results from ATom and HIPPO suggest that deep convection can

426   loft O_3-poor air at least up to 12 km (the altitude ceiling of this study) in the tropical Pacific, and

427   occurred more frequently between January and May (Figs. 12c and h). During the rest of the

428   year, O_3-poor air was typically confined below 4 km. Conversely, O_3-poor air is confined to the

429   first 2 km in the tropical Atlantic (Fig. S5). Meteorological analysis of tropical ozonesondes

430   shows that subsidence of higher-O_3 air aloft over the Atlantic is one reason O_3-poor air is found

431   only in the boundary layer (Thompson et al., 2000, 2012).

432

433   4.2. Middle- and high-latitudes

434   **Vertical distribution.** In the middle- and high-latitudes, tropospheric O_3 was generally at

435   a minimum in the MBL and increased with altitude. Above 8 km, increasing O_3 with altitude

436   (Figs. 10b–e) and its persistent anticorrelation with CO (Fig. 13) points to stratospheric air

437   sampling as the cause for higher O_3 variability in the extra-tropical UTLS, especially at high

438   latitudes where the tropopause is lower and wave breaking of the polar jet streams can lead to

439   stratospheric intrusions. As a result, the S_{score} decrease above 8 km, summarized in Figure 11a, is

440   ascribed to variability in the influence of stratospheric air. ATom detected little change in the O_3

441   distribution over the Pacific Ocean since HIPPO, with a S_{score} averaging 74 % in the 0–8 km

442   range. The relative difference between median O_3 values from HIPPO and ATom in the Pacific

443   is generally lower than 20 % (Fig. 11b). Similarly, the relative difference between median O_3

444   mixing ratios between ATom Atlantic and Pacific below 8 km is consistently lower than 20 %,

445   with an average S_{score} of 75 % between (Fig. 11b). The southern high-latitudes are the only

446   region where the S_{score} below 8 km occasionally fell below 60 % (Fig. 10e). However, a lower

447   S_{score} was expected there as the Atlantic vertical profile is based on only two seasonal flights to

448   Antarctica, whereas there were four seasonal flights in the Pacific. Additionally, HIPPO was less

449   spatially extensive – resulting in fewer data points – in this latitude bin compared to ATom (Fig.

450   1), which could explain the low S_{score} values when comparing the two missions (Fig. 10e).

451   Nevertheless, the similar O_3 distribution in the extra-tropical free troposphere above the two

452   oceans is consistent with an O_3 lifetime sufficiently long for rapid zonal transport to smooth out

453   variations in baseline O_3 distribution in the remote troposphere, across a relatively wide range of

454   longitudes (Figs. 10b–e). The comparison of O_3 seasonal cycles at remote ozonesonde launching

455   sites of the northern midlatitudes yields similar results and further supports this conclusion

456   (Parrish et al., in review). Studies of the spatial representativeness of tropospheric O_3 monitoring

457   networks have concluded that tropospheric O_3 distributions varied significantly with longitude,

458   especially in the northern middle- and high-latitudes over continents (Liu et al., 2013; Tilmes et

459   al., 2012). ATom findings stem from O_3 measurements predominantly over the oceans, possibly

460   yielding a different picture of O_3 longitudinal distribution away from regional precursor

461   emissions.

462   **Seasonality.** The extra-tropical vertical profiles of O_3 vary seasonally during ATom and

463   HIPPO. The summer season in the middle- and high-latitudes was remarkable over both oceans

464   and hemispheres for the steep O_3 gradients in the tropospheric column (Fig. 12 in black). In the

465   MBL, median O_3 was consistently under 25 ppbv in the summer, whereas O_3 was over 25 ppbv

466   in other seasons. Low O_3 in the MBL in summer reflects the enhanced O_3 photochemical

467   destruction in this NO_x-limited region. Photochemical destruction decreases in dry air in the

468   upper troposphere, thus leading to the steep O_3 gradients observed here. The summer O_3

469   minimum was especially apparent in the high latitudes of the southern Pacific during ATom and

470   extended well above the MBL into the free troposphere (Fig. 12 in black).

471   O_3 mixing ratios were highest in the tropospheric column during springtime in both

472   hemispheres, and over both oceans (Fig. 12 in gold). A notable exception occurred during

473   springtime in the high latitudes of the NH, where several O_3 depletion events were sampled in

474   the lower legs of the Arctic transit. During these events, O_3 mixing ratios lower than 10 ppbv

475   were measured, resulting in a lower 25th percentile of O_3 distribution at the lowest altitude

476   compared to the other seasons (Fig. 12e in gold). A tropospheric O_3 springtime maximum has

477   often been reported in the NH (e.g., Monks, 2000) when meteorology favors efficient transport

478   of O_3 and precursors from continental air from North America and Eurasia (Owen et al., 2006;

479   Zhang et al., 2017, 2008). Another contributing factor is the increased frequency of stratospheric

480   air mixing in spring that significantly contributes to higher O_3 levels (Lin et al., 2015; Tarasick et

481   al., 2019b). Further, the tropospheric O_3 springtime maximum in the SH is often attributed to BB

482   emissions reaching a peak ((Fishman et al., 1991; Gaudel et al., 2018), but stratospheric air

483   mixing also occurs (Diab et al., 1996, 2004; Greenslade et al., 2017). Here, the O_3/CO

484   relationship in spring shows that the enhanced stratospheric mixing with tropospheric air during

485   this season, both in the northern and southern middle- and high-latitudes, contributes to the

486   increase in column O_3 (Fig. 13).

487   Fall and winter seasons shared similar features in the middle- and high-latitudes: no

488   strong O_3 gradient was measured in the free troposphere, and O_3 values varied over similar

489   ranges – about 40 ppbv in the NH and about 30 ppbv in the SH – during the two seasons (Fig. 12

490   in red and blue).

491   **O_3 enhancements.** The linear increase of O_3 with CO >100 ppbv highlights the

492   contribution of natural and anthropogenic pollution plumes lofted from continental areas into the

493   remote troposphere.

494   In the NH, these events occur almost year-round (Figs. 13b–c and 13g–h). Higher CO

495   enhancements in the Pacific (Figs. 13g–h) than in the Atlantic (Figs. 13b–c) have been observed

496   before and attributed to sampling bias (Clark et al., 2015). Here, our findings suggest a year-

497   round influence of continental emissions on the Pacific atmosphere despite its remoteness.

498   Modeled back trajectories show that most air masses sampled in the NH during ATom were

499   influenced by long-range transport of continental emissions from Asia, Africa, and North

500   America (Fig. S6). Previous studies have shown anthropogenic and BB emission outflow from

501   Asia significantly contributed to O_3 pollution events measured over the northern Pacific or in

502   California (e.g., Heald et al., 2003; Jaffe et al., 2004; Lin et al., 2017). Intercontinental transport

503   of anthropogenic emissions from Europe can also contribute to the Asian outflow of

504   anthropogenic pollution (e.g., Bey et al., 2001; Liu et al., 2002; Newell and Evans, 2000).

505   Finally, O_3 enhancements in the northern Atlantic were frequently observed and attributed to

506   midlatitude anthropogenic and boreal forest fire emissions (e.g., Honrath et al., 2004; Martín et

507   al., 2006; Trickl et al., 2003).

508   In the SH, polluted air is encountered more often in spring and summer over the Atlantic,

509   but springtime CO is greater than in other seasons over the Pacific (Figs. 13d–e and 13i–j).

510   During spring, median O_3 above 50 ppbv was measured throughout the free troposphere in the

511   southern midlatitudes (Fig. 12). Several air masses intercepted during these flights originated

512   from regions that were intensively burning at the time, notably equatorial and southern Africa,

513   Australia, and southern South America, contributing to the observed enhanced O_3 and CO (Fig.

514   S4).

515

516   **5. Conclusion**

517   We present tropospheric O_3 distributions measured over remote regions of the Pacific and

518   Atlantic Oceans during two airborne chemical sampling projects: the four deployments of ATom

519   (2016–2018) and the five deployments of HIPPO (2009–2011). The data highlight several

520   regional- and large-scale features of O_3 distributions, and provide valuable new insight into O_3

521   distributions in remote regions. The main findings are as follows:

522   -   ATom and HIPPO provide a unique perspective on vertically-resolved global baseline O_3

523   distributions over the Pacific and Atlantic basins, and expand upon spatially-limited O_3

524   climatologies from long-term datasets to highlight large-scale features necessary for

525   model output and satellite retrieval validation.

526   -   ATom and HIPPO O_3 data are consistent – where they overlap – with measurement-

527   based climatologies of tropospheric O_3 from well-established ozonesonde and

528   commercial aircraft monitoring programs. ATom and HIPPO seasonal median O_3 showed

529   high correlation ($R^2 > 0.7$) with corresponding seasonal median O_3 from ozonesondes,

530   giving confidence in the accurate depiction of the emerging global O_3 climatology by

531   these diverse research activities.

532   ATom and HIPPO captured 30–71 % of O_3 variability measured by ozonesondes

533   launched in the vicinity of the aircraft flight tracks, and had the same mode of the O_3

534   distribution as determined by IAGOS in the northern Atlantic UTLS.

535 - Higher O_3 loading in the NH compared to the SH is consistent with the heterogeneous

536   distribution of O_3 precursor emissions around the globe, mostly concentrated in the NH.

537   ATom Atlantic vs. Pacific comparison reveals a similar O_3 distribution in the free

538   troposphere up to ~8 km in the middle- and high-latitudes, but not in the tropics. In the

539   tropics, median O_3 mixing ratios are about twice as high in the Atlantic than in the

540   Pacific, due to a well-documented mixture of dynamical patterns interacting with the

541   transport of continental air masses.

542 - The comparison of seasonal O_3 vertical profiles does not reveal a marked seasonality in

543   the tropics, but instead highlights the influence of specific events, most notably BB

544   emissions from Africa and South America. In the extra-tropics, the summer season is

545   characterized by a steeper tropospheric O_3 gradient driven by very low O_3 abundance in

546   the MBL. Fall and winter seasons generally lead to near-constant O_3 mixing ratios from

547   the surface to the upper troposphere, while the highest O_3 abundance is recorded during

548   the spring season when more frequent and intense stratospheric intrusions and transport

549   of air masses from continental regions occur.

550 - Overall, this paper highlights the value of the ATom and HIPPO datasets, which cover

551   spatial scales commensurate with the grid resolution of current Earth system models, and

552   further useful as a priori estimates for improved retrievals of tropospheric O_3 from

553   satellite remote sensing platforms. ATom and HIPPO datasets should be critical for

554   improving the scientific community's understanding of O_3 production and loss processes,

555   and the influence of anthropogenic emissions on baseline O_3 in remote regions. They

556   provide a timely addition to the Tropospheric Ozone Assessment Report (TOAR) effort

557   to characterize the global-scale O_3 distribution, and addresses some of the measurement

558   gaps identified therein.

559

Acknowledgments

We thank the ATom leadership team, science team, and DC-8 pilots and crew for contributions
to the ATom measurements. The authors acknowledge support by the U.S. NASA's Earth
System Science Pathfinder Program under award NNH15AB12I, NNX15AJ23G and
NNX15AH33A, and by the U.S. National Oceanic and Atmospheric Administration (NOAA)
Health of the Atmosphere and Atmospheric Chemistry, Carbon Cycle, and Climate Programs.
SHADOZ ozonesondes are supported by the Upper Atmosphere Research Program of NASA.
Ozonesoundings at Marambio have been supported by the Finnish Antarctic research program
(FINNARP). We thank J. A. Neuman, H. Angot, and O. Cooper for helpful discussions and
careful editing of this manuscript. The IAGOS program acknowledges the European
Commission for its support of the MOZAIC project (1994-2003) the preparatory phase of
IAGOS (2005-2013) and IGAS (2013-2016); the partner institutions of the IAGOS Research
Infrastructure (FZJ, DLR, MPI, KIT in Germany, CNRS, Météo-France, Université Paul Sabatier
in France, and University of Manchester, UK); the French Atmospheric Data Center AERIS for
hosting the database; and the participating airlines (Lufthansa, Air France, China Airlines, Iberia,
Cathay Pacific, Hawaiian Airlines) for transporting the instrumentation free of charge.

References

Andreae, M. O., Anderson, B. E., Blake, D. R., Bradshaw, J. D., Collins, J. E., Gregory, G. L.,
Sachse, G. W. and Shipham, M. C.: Influence of plumes from biomass burning on atmospheric
chemistry over the equatorial and tropical South Atlantic during CITE 3, Journal of Geophysical
Research, 99(D6), 12793, doi:10.1029/94JD00263, 1994.

Bey, I., Jacob, D. J., Logan, J. A. and Yantosca, R. M.: Asian chemical outflow to the Pacific in
spring: Origins, pathways, and budgets, Journal of Geophysical Research: Atmospheres,
106(D19), 23097–23113, doi:10.1029/2001JD000806, 2001.

Bowman, K. P.: Large-scale isentropic mixing properties of the Antarctic polar vortex from
analyzed winds, Journal of Geophysical Research: Atmospheres, 98(D12), 23013–23027,
doi:10.1029/93JD02599, 1993.

Bowman, K. P. and Carrie, G. D.: The Mean-Meridional Transport Circulation of the Troposphere
in an Idealized GCM, J. Atmos. Sci., 59(9), 1502–1514, doi:10.1175/1520-
0469(2002)059<1502:TMMTCO>2.0.CO;2, 2002.

593 Brenninkmeijer, C. a. M., Crutzen, P., Boumard, F., Dauer, T., Dix, B., Ebinghaus, R., Filippi, D.,
594 Fischer, H., Franke, H., Frieβ, U., Heintzenberg, J., Helleis, F., Hermann, M., Kock, H. H., Koeppel,
595 C., Lelieveld, J., Leuenberger, M., Martinsson, B. G., Miemczyk, S., Moret, H. P., Nguyen, H. N.,
596 Nyfeler, P., Oram, D., O'Sullivan, D., Penkett, S., Platt, U., Pupek, M., Ramonet, M., Randa, B.,
597 Reichelt, M., Rhee, T. S., Rohwer, J., Rosenfeld, K., Scharffe, D., Schlager, H., Schumann, U.,
598 Slemr, F., Sprung, D., Stock, P., Thaler, R., Valentino, F., Velthoven, P. van, Waibel, A., Wandel,
599 A., Waschitschek, K., Wiedensohler, A., Xueref-Remy, I., Zahn, A., Zech, U. and Ziereis, H.: Civil
600 Aircraft for the regular investigation of the atmosphere based on an instrumented container:
601 The new CARIBIC system, Atmospheric Chemistry and Physics, 7(18), 4953–4976,
602 doi:https://doi.org/10.5194/acp-7-4953-2007, 2007.

603 Clark, H., Sauvage, B., Thouret, V., Nédélec, P., Blot, R., Wang, K.-Y., Smit, H., Neis, P., Petzold,
604 A., Athier, G., Boulanger, D., Cousin, J.-M., Beswick, K., Gallagher, M., Baumgardner, D., Kaiser,
605 J., Flaud, J.-M., Wahner, A., Volz-Thomas, A. and Cammas, J.-P.: The first regular measurements
606 of ozone, carbon monoxide and water vapour in the Pacific UTLS by IAGOS, Tellus B: Chemical
607 and Physical Meteorology, 67(1), 28385, doi:10.3402/tellusb.v67.28385, 2015.

608 Cohen, Y., Petetin, H., Thouret, V., Marécal, V., Josse, B., Clark, H., Sauvage, B., Fontaine, A.,
609 Athier, G., Blot, R., Boulanger, D., Cousin, J.-M. and Nédélec, P.: Climatology and long-term
610 evolution of ozone and carbon monoxide in the upper troposphere–lower stratosphere (UTLS)
611 at northern midlatitudes, as seen by IAGOS from 1995 to 2013, Atmospheric Chemistry and
612 Physics, 18(8), 5415–5453, doi:https://doi.org/10.5194/acp-18-5415-2018, 2018.

613 Cooper, O. R., Stohl, A., Hübler, G., Hsie, E. Y., Parrish, D. D., Tuck, A. F., Kiladis, G. N., Oltmans,
614 S. J., Johnson, B. J., Shapiro, M., Moody, J. L. and Lefohn, A. S.: Direct transport of midlatitude
615 stratospheric ozone into the lower troposphere and marine boundary layer of the tropical
616 Pacific Ocean, J. Geophys. Res., 110(D23), D23310, doi:10.1029/2005JD005783, 2005.

617 Crutzen, P. J.: Photochemical reactions initiated by and influencing ozone in unpolluted
618 tropospheric air, Tellus, 26(1–2), 47–57, doi:10.3402/tellusa.v26i1-2.9736, 1974.

619 Diab, R. D., Thompson, A. M., Zunckel, M., Coetzee, G. J. R., Combrink, J., Bodeker, G. E.,
620 Fishman, J., Sokolic, F., McNamara, D. P., Archer, C. B. and Nganga, D.: Vertical ozone
621 distribution over southern Africa and adjacent oceans during SAFARI-92, Journal of Geophysical
622 Research: Atmospheres, 101(D19), 23823–23833, doi:10.1029/96JD01267, 1996.

623 Diab, R. D., Thompson, A. M., Mari, K., Ramsay, L. and Coetzee, G. J. R.: Tropospheric ozone
624 climatology over Irene, South Africa, from 1990 to 1994 and 1998 to 2002, Journal of
625 Geophysical Research: Atmospheres, 109(D20), doi:10.1029/2004JD004793, 2004.

626 Fan, S.-M. and Jacob, D. J.: Surface ozone depletion in Arctic spring sustained by bromine
627 reactions on aerosols, Nature, 359(6395), 522–524, doi:10.1038/359522a0, 1992.

628 Fishman, J., Fakhruzzaman, K., Cros, B. and Nganga, D.: Identification of Widespread Pollution in
629 the Southern Hemisphere Deduced from Satellite Analyses, Science, 252(5013), 1693–1696,
630 doi:10.1126/science.252.5013.1693, 1991.

631 Fishman, J., Hoell, J. M., Bendura, R. D., McNeal, R. J. and Kirchhoff, V. W. J. H.: NASA GTE
632 TRACE A experiment (September–October 1992): Overview, Journal of Geophysical Research:
633 Atmospheres, 101(D19), 23865–23879, doi:10.1029/96JD00123, 1996.

634 Gaudel, A., Clark, H., Thouret, V., Jones, L., Inness, A., Flemming, J., Stein, O., Huijnen, V., Eskes,
635 H., Nedelec, P. and Boulanger, D.: On the use of MOZAIC-IAGOS data to assess the ability of the
636 MACC reanalysis to reproduce the distribution of ozone and CO in the UTLS over Europe, Tellus
637 B: Chemical and Physical Meteorology, 68(s1), 27955, doi:10.3402/tellusb.v67.27955, 2015.

638 Gaudel, A., Cooper, O. R., Ancellet, G., Barret, B., Boynard, A., Burrows, J. P., Clerbaux, C.,
639 Coheur, P.-F., Cuesta, J., Cuevas, E., Doniki, S., Dufour, G., Ebojie, F., Foret, G., Garcia, O.,
640 Muños, M. J. G., Hannigan, J. W., Hase, F., Huang, G., Hassler, B., Hurtmans, D., Jaffe, D., Jones,
641 N., Kalabokas, P., Kerridge, B., Kulawik, S. S., Latter, B., Leblanc, T., Flochmoën, E. L., Lin, W., Liu,
642 J., Liu, X., Mahieu, E., McClure-Begley, A., Neu, J. L., Osman, M., Palm, M., Petetin, H.,
643 Petropavlovskikh, I., Querel, R., Rahpoe, N., Rozanov, A., Schultz, M. G., Schwab, J., Siddans, R.,
644 Smale, D., Steinbacher, M., Tanimoto, H., Tarasick, D. W., Thouret, V., Thompson, A. M., Trickl,
645 T., Weatherhead, E., Wespes, C., Worden, H. M., Vigouroux, C., Xu, X., Zeng, G. and Ziemke, J.:
646 Tropospheric Ozone Assessment Report: Present-day distribution and trends of tropospheric
647 ozone relevant to climate and global atmospheric chemistry model evaluation, Elem Sci Anth,
648 6(1), doi:10.1525/elementa.291, 2018.

649 Greenslade, J. W., Alexander, S. P., Schofield, R., Fisher, J. A. and Klekociuk, A. K.: Stratospheric
650 ozone intrusion events and their impacts on tropospheric ozone in the Southern Hemisphere,
651 Atmospheric Chemistry and Physics, 17(17), 10269–10290, doi:10.5194/acp-17-10269-2017,
652 2017.

653 Heald, C. L., Jacob, D. J., Fiore, A. M., Emmons, L. K., Gille, J. C., Deeter, M. N., Warner, J.,
654 Edwards, D. P., Crawford, J. H., Hamlin, A. J., Sachse, G. W., Browell, E. V., Avery, M. A., Vay, S.
655 A., Westberg, D. J., Blake, D. R., Singh, H. B., Sandholm, S. T., Talbot, R. W. and Fuelberg, H. E.:
656 Asian outflow and trans-Pacific transport of carbon monoxide and ozone pollution: An
657 integrated satellite, aircraft, and model perspective, Journal of Geophysical Research:
658 Atmospheres, 108(D24), doi:10.1029/2003JD003507, 2003.

659 Holmes, C. D., Prather, M. J., Søvde, O. A. and Myhre, G.: Future methane, hydroxyl, and their
660 uncertainties: key climate and emission parameters for future predictions, Atmos. Chem. Phys.,
661 13(1), 285–302, doi:10.5194/acp-13-285-2013, 2013.

662 Honrath, R. E., Owen, R. C., Martín, M. V., Reid, J. S., Lapina, K., Fialho, P., Dziobak, M. P., Kleissl,
663 J. and Westphal, D. L.: Regional and hemispheric impacts of anthropogenic and biomass burning
664 emissions on summertime CO and O3 in the North Atlantic lower free troposphere, Journal of
665 Geophysical Research: Atmospheres, 109(D24), doi:10.1029/2004JD005147, 2004.

666   IPCC: Climate Change 2013: The Physical Science Basis. Contribution of Working Group I to the
667   Fifth Assessment Report of the Intergovernmental Panel on Climate Change, Cambridge
668   University Press, Cambridge, United Kingdom and New York, NY, USA. [online] Available from:
669   https://www.ipcc.ch/report/ar5/wg1/ (Accessed 8 January 2019), 2013.

670   Jaffe, D., Bertschi, I., Jaeglé, L., Novelli, P., Reid, J. S., Tanimoto, H., Vingarzan, R. and Westphal,
671   D. L.: Long-range transport of Siberian biomass burning emissions and impact on surface ozone
672   in western North America, Geophysical Research Letters, 31(16), doi:10.1029/2004GL020093,
673   2004.

674   Jensen, A. A., Thompson, A. M. and Schmidlin, F. J.: Classification of Ascension Island and Natal
675   ozonesondes using self-organizing maps, Journal of Geophysical Research: Atmospheres,
676   117(D4), doi:10.1029/2011JD016573, 2012.

677   Jourdain, L., Worden, H. M., Worden, J. R., Bowman, K., Li, Q., Eldering, A., Kulawik, S. S.,
678   Osterman, G., Boersma, K. F., Fisher, B., Rinsland, C. P., Beer, R. and Gunson, M.: Tropospheric
679   vertical distribution of tropical Atlantic ozone observed by TES during the northern African
680   biomass burning season, Geophysical Research Letters, 34(4), doi:10.1029/2006GL028284,
681   2007.

682   Junge, C. E.: Global ozone budget and exchange between stratosphere and troposphere, Tellus,
683   14(4), 363–377, doi:10.1111/j.2153-3490.1962.tb01349.x, 1962.

684   Karion, A., Sweeney, C., Wolter, S., Newberger, T., Chen, H., Andrews, A., Kofler, J., Neff, D. and
685   Tans, P.: Long-term greenhouse gas measurements from aircraft, Atmospheric Measurement
686   Techniques, 6(3), 511–526, doi:https://doi.org/10.5194/amt-6-511-2013, 2013.

687   Katich, J. M., Samset, B. H., Bui, T. P., Dollner, M., Froyd, K. D., Campuzano-Jost, P., Nault, B. A.,
688   Schroder, J. C., Weinzierl, B. and Schwarz, J. P.: Strong Contrast in Remote Black Carbon Aerosol
689   Loadings Between the Atlantic and Pacific Basins, Journal of Geophysical Research:
690   Atmospheres, 123(23), 13,386-13,395, doi:10.1029/2018JD029206, 2018.

691   Kley, D., Crutzen, P. J., Smit, H. G. J., Vömel, H., Oltmans, S. J., Grassl, H. and Ramanathan, V.:
692   Observations of Near-Zero Ozone Concentrations Over the Convective Pacific: Effects on Air
693   Chemistry, Science, 274(5285), 230–233, doi:10.1126/science.274.5285.230, 1996.

694   Komhyr, W.: Electrochemical Concentration Cells for Gas Analysis, Annales De Geophysique,
695   25(1), 203-, 1969.

696   Krishnamurti, T. N., Sinha, M. C., Kanamitsu, M., Oosterhof, D., Fuelberg, H., Chatfield, R., Jacob,
697   D. J. and Logan, J.: Passive tracer transport relevant to the TRACE A experiment, Journal of
698   Geophysical Research: Atmospheres, 101(D19), 23889–23907, doi:10.1029/95JD02419, 1996.

699   Leonard, M., Petropavlovskikh, I., Lin, M., McClure-Begley, A., Johnson, B. J., Oltmans, S. J. and
700   Tarasick, D.: An assessment of 10-year NOAA aircraft-based tropospheric ozone profiling in

701 Colorado, Atmospheric Environment, 158, 116–127, doi:10.1016/j.atmosenv.2017.03.013,
702 2017.

703 Levy, H.: Normal Atmosphere: Large Radical and Formaldehyde Concentrations Predicted,
704 Science, 173(3992), 141–143, doi:10.1126/science.173.3992.141, 1971.

705 Lin, M., Fiore, A. M., Horowitz, L. W., Langford, A. O., Oltmans, S. J., Tarasick, D. and Rieder, H.
706 E.: Climate variability modulates western US ozone air quality in spring via deep stratospheric
707 intrusions, Nature Communications, 6, 7105, doi:10.1038/ncomms8105, 2015.

708 Lin, M., Horowitz, L. W., Payton, R., Fiore, A. M. and Tonnesen, G.: US surface ozone trends and
709 extremes from 1980 to 2014: quantifying the roles of rising Asian emissions, domestic controls,
710 wildfires, and climate, Atmospheric Chemistry and Physics, 17(4), 2943–2970, doi:10.5194/acp-
711 17-2943-2017, 2017.

712 Liu, G., Tarasick, D. W., Fioletov, V. E., Sioris, C. E. and Rochon, Y. J.: Ozone correlation lengths
713 and measurement uncertainties from analysis of historical ozonesonde data in North America
714 and Europe, Journal of Geophysical Research: Atmospheres, 114(D4),
715 doi:10.1029/2008JD010576, 2009.

716 Liu, G., Liu, J., Tarasick, D. W., Fioletov, V. E., Jin, J. J., Moeini, O., Liu, X., Sioris, C. E. and Osman,
717 M.: A global tropospheric ozone climatology from trajectory-mapped ozone soundings,
718 Atmospheric Chemistry and Physics, 13(21), 10659–10675, doi:10.5194/acp-13-10659-2013,
719 2013.

720 Liu, H., Jacob, D. J., Chan, L. Y., Oltmans, S. J., Bey, I., Yantosca, R. M., Harris, J. M., Duncan, B. N.
721 and Martin, R. V.: Sources of tropospheric ozone along the Asian Pacific Rim: An analysis of
722 ozonesonde observations, Journal of Geophysical Research: Atmospheres, 107(D21), ACH 3-1-
723 ACH 3-19, doi:10.1029/2001JD002005, 2002.

724 Marenco, A., Thouret, V., Nédélec, P., Smit, H., Helten, M., Kley, D., Karcher, F., Simon, P., Law,
725 K., Pyle, J., Poschmann, G., Wrede, R. V., Hume, C. and Cook, T.: Measurement of ozone and
726 water vapor by Airbus in-service aircraft: The MOZAIC airborne program, an overview, Journal
727 of Geophysical Research: Atmospheres, 103(D19), 25631–25642, doi:10.1029/98JD00977,
728 1998.

729 Martín, M. V., Honrath, R. E., Owen, R. C., Pfister, G., Fialho, P. and Barata, F.: Significant
730 enhancements of nitrogen oxides, black carbon, and ozone in the North Atlantic lower free
731 troposphere resulting from North American boreal wildfires, Journal of Geophysical Research:
732 Atmospheres, 111(D23), doi:10.1029/2006JD007530, 2006.

733 Monks, P. S.: A review of the observations and origins of the spring ozone maximum,
734 Atmospheric Environment, 34(21), 3545–3561, doi:10.1016/S1352-2310(00)00129-1, 2000.

735 Monks, P. S., Carpenter, L. J., Penkett, S. A., Ayers, G. P., Gillett, R. W., Galbally, I. E. and (Mick)
736 Meyer, C. P.: Fundamental ozone photochemistry in the remote marine boundary layer: the

737   soapex experiment, measurement and theory, Atmospheric Environment, 32(21), 3647–3664,
738   doi:10.1016/S1352-2310(98)00084-3, 1998.

739   Monks, P. S., Salisbury, G., Holland, G., Penkett, S. A. and Ayers, G. P.: A seasonal comparison of
740   ozone photochemistry in the remote marine boundary layer, Atmospheric Environment, 34(16),
741   2547–2561, doi:10.1016/S1352-2310(99)00504-X, 2000.

742   Monks, P. S., Granier, C., Fuzzi, S., Stohl, A., Williams, M. L., Akimoto, H., Amann, M., Baklanov,
743   A., Baltensperger, U., Bey, I., Blake, N., Blake, R. S., Carslaw, K., Cooper, O. R., Dentener, F.,
744   Fowler, D., Fragkou, E., Frost, G. J., Generoso, S., Ginoux, P., Grewe, V., Guenther, A., Hansson,
745   H. C., Henne, S., Hjorth, J., Hofzumahaus, A., Huntrieser, H., Isaksen, I. S. A., Jenkin, M. E.,
746   Kaiser, J., Kanakidou, M., Klimont, Z., Kulmala, M., Laj, P., Lawrence, M. G., Lee, J. D., Liousse, C.,
747   Maione, M., McFiggans, G., Metzger, A., Mieville, A., Moussiopoulos, N., Orlando, J. J., O'Dowd,
748   C. D., Palmer, P. I., Parrish, D. D., Petzold, A., Platt, U., Pöschl, U., Prévôt, A. S. H., Reeves, C. E.,
749   Reimann, S., Rudich, Y., Sellegri, K., Steinbrecher, R., Simpson, D., ten Brink, H., Theloke, J., van
750   der Werf, G. R., Vautard, R., Vestreng, V., Vlachokostas, Ch. and von Glasow, R.: Atmospheric
751   composition change – global and regional air quality, Atmospheric Environment, 43(33), 5268–
752   5350, doi:10.1016/j.atmosenv.2009.08.021, 2009.

753   Moxim, W. J. and Levy, H.: A model analysis of the tropical South Atlantic Ocean tropospheric
754   ozone maximum: The interaction of transport and chemistry, Journal of Geophysical Research:
755   Atmospheres, 105(D13), 17393–17415, doi:10.1029/2000JD900175, 2000.

756   Nath, D., Chen, W., Graf, H.-F., Lan, X., Gong, H., Nath, R., Hu, K. and Wang, L.: Subtropical
757   Potential Vorticity Intrusion Drives Increasing Tropospheric Ozone over the Tropical Central
758   Pacific, Scientific Reports, 6, 21370, doi:10.1038/srep21370, 2016.

759   Nédélec, P., Cammas, J.-P., Thouret, V., Athier, G., Cousin, J.-M., Legrand, C., Abonnel, C.,
760   Lecoeur, F., Cayez, G. and Marizy, C.: An improved infrared carbon monoxide analyser for
761   routine measurements aboard commercial Airbus aircraft: technical validation and first
762   scientific results of the MOZAIC III programme, Atmospheric Chemistry and Physics, 3(5), 1551–
763   1564, doi:https://doi.org/10.5194/acp-3-1551-2003, 2003.

764   Nédélec, P., Blot, R., Boulanger, D., Athier, G., Cousin, J.-M., Gautron, B., Petzold, A., Volz-
765   Thomas, A. and Thouret, V.: Instrumentation on commercial aircraft for monitoring the
766   atmospheric composition on a global scale: the IAGOS system, technical overview of ozone and
767   carbon monoxide measurements, Tellus B: Chemical and Physical Meteorology, 68(s1), 27791,
768   doi:10.3402/tellusb.v67.27791, 2015.

769   Neuman, J. A., Trainer, M., Aikin, K. C., Angevine, W. M., Brioude, J., Brown, S. S., de Gouw, J. A.,
770   Dube, W. P., Flynn, J. H., Graus, M., Holloway, J. S., Lefer, B. L., Nedelec, P., Nowak, J. B., Parrish,
771   D. D., Pollack, I. B., Roberts, J. M., Ryerson, T. B., Smit, H., Thouret, V. and Wagner, N. L.:
772   Observations of ozone transport from the free troposphere to the Los Angeles basin, Journal of
773   Geophysical Research: Atmospheres, 117(D21), n/a-n/a, doi:10.1029/2011JD016919, 2012.

774   Newell, R. E. and Evans, M. J.: Seasonal changes in pollutant transport to the North Pacific: The
775   relative importance of Asian and European sources, Geophysical Research Letters, 27(16),
776   2509–2512, doi:10.1029/2000GL011501, 2000.

777   Oltmans, S. J., Johnson, B. J., Harris, J. M., Vömel, H., Thompson, A. M., Koshy, K., Simon, P.,
778   Bendura, R. J., Logan, J. A., Hasebe, F., Shiotani, M., Kirchhoff, V. W. J. H., Maata, M., Sami, G.,
779   Samad, A., Tabuadravu, J., Enriquez, H., Agama, M., Cornejo, J. and Paredes, F.: Ozone in the
780   Pacific tropical troposphere from ozonesonde observations, Journal of Geophysical Research:
781   Atmospheres, 106(D23), 32503–32525, doi:10.1029/2000JD900834, 2001.

782   Oltmans, S. J., Lefohn, A. S., Shadwick, D., Harris, J. M., Scheel, H. E., Galbally, I., Tarasick, D. W.,
783   Johnson, B. J., Brunke, E.-G., Claude, H., Zeng, G., Nichol, S., Schmidlin, F., Davies, J., Cuevas, E.,
784   Redondas, A., Naoe, H., Nakano, T. and Kawasato, T.: Recent tropospheric ozone changes – A
785   pattern dominated by slow or no growth, Atmospheric Environment, 67, 331–351,
786   doi:10.1016/j.atmosenv.2012.10.057, 2013.

787   Owen, R. C., Cooper, O. R., Stohl, A. and Honrath, R. E.: An analysis of the mechanisms of North
788   American pollutant transport to the central North Atlantic lower free troposphere, Journal of
789   Geophysical Research: Atmospheres, 111(D23), doi:10.1029/2006JD007062, 2006.

790   Pan, L. L., Honomichl, S. B., Randel, W. J., Apel, E. C., Atlas, E. L., Beaton, S. P., Bresch, J. F.,
791   Hornbrook, R., Kinnison, D. E., Lamarque, J.-F., Saiz-Lopez, A., Salawitch, R. J. and Weinheimer,
792   A. J.: Bimodal distribution of free tropospheric ozone over the tropical western Pacific revealed
793   by airborne observations, Geophysical Research Letters, 42(18), 7844–7851,
794   doi:10.1002/2015GL065562, 2015.

795   Parrish, Galbally I. E., Lamarque J.-F., Naik V., Horowitz L., Shindell D. T., Oltmans S. J., Derwent
796   R., Tanimoto H., Labuschagne C. and Cupeiro M.: Seasonal cycles of O3 in the marine boundary
797   layer: Observation and model simulation comparisons, Journal of Geophysical Research:
798   Atmospheres, 121(1), 538–557, doi:10.1002/2015JD024101, 2016.

799   Perkins, S. E., Pitman, A. J., Holbrook, N. J. and McAneney, J.: Evaluation of the AR4 Climate
800   Models' Simulated Daily Maximum Temperature, Minimum Temperature, and Precipitation
801   over Australia Using Probability Density Functions, J. Climate, 20(17), 4356–4376,
802   doi:10.1175/JCLI4253.1, 2007.

803   Petzold, A., Thouret, V., Gerbig, C., Zahn, A., Brenninkmeijer, C. A. M., Gallagher, M., Hermann,
804   M., Pontaud, M., Ziereis, H., Boulanger, D., Marshall, J., Nédélec, P., Smit, H. G. J., Friess, U.,
805   Flaud, J.-M., Wahner, A., Cammas, J.-P., Volz-Thomas, A. and TEAM, I.: Global-scale atmosphere
806   monitoring by in-service aircraft – current achievements and future prospects of the European
807   Research Infrastructure IAGOS, Tellus B: Chemical and Physical Meteorology, 67(1), 28452,
808   doi:10.3402/tellusb.v67.28452, 2015.

809   Pickering, K. E., Thompson, A. M., Wang, Y., Tao, W.-K., McNamara, D. P., Kirchhoff, V. W. J. H.,
810   Heikes, B. G., Sachse, G. W., Bradshaw, J. D., Gregory, G. L. and Blake, D. R.: Convective

811 transport of biomass burning emissions over Brazil during TRACE A, Journal of Geophysical
812 Research: Atmospheres, 101(D19), 23993–24012, doi:10.1029/96JD00346, 1996.

813 Proffitt, M. H. and McLaughlin, R. J.: Fast-response dual-beam UV-absorption ozone
814 photometer suitable for use on stratospheric balloons, Review of Scientific Instruments, 54(12),
815 1719–1728, doi:10.1063/1.1137316, 1983.

816 Ridley, B. A., Grahek, F. E. and Walega, J. G.: A Small High-Sensitivity, Medium-Response Ozone
817 Detector Suitable for Measurements from Light Aircraft, J. Atmos. Oceanic Technol., 9(2), 142–
818 148, doi:10.1175/1520-0426(1992)009<0142:ASHSMR>2.0.CO;2, 1992.

819 Santoni, G. W., Daube, B. C., Kort, E. A., Jiménez, R., Park, S., Pittman, J. V., Gottlieb, E., Xiang,
820 B., Zahniser, M. S., Nelson, D. D., McManus, J. B., Peischl, J., Ryerson, T. B., Holloway, J. S.,
821 Andrews, A. E., Sweeney, C., Hall, B., Hintsa, E. J., Moore, F. L., Elkins, J. W., Hurst, D. F.,
822 Stephens, B. B., Bent, J. and Wofsy, S. C.: Evaluation of the airborne quantum cascade laser
823 spectrometer (QCLS) measurements of the carbon and greenhouse gas suite – CO_2, CH_4,
824 N_2O, and CO – during the CalNex and HIPPO campaigns, Atmospheric Measurement
825 Techniques, 7(6), 1509–1526, doi:https://doi.org/10.5194/amt-7-1509-2014, 2014.

826 Sauvage, B., Thouret, V., Thompson, A. M., Witte, J. C., Cammas, J.-P., Nédélec, P. and Athier,
827 G.: Enhanced view of the "tropical Atlantic ozone paradox" and "zonal wave one" from the in
828 situ MOZAIC and SHADOZ data, Journal of Geophysical Research: Atmospheres, 111(D1),
829 doi:10.1029/2005JD006241, 2006.

830 Shen, Z., Liu, J., Horowitz, L. W., Henze, D. K., Fan, S., H., L. I., Mauzerall, D. L., Lin, J.-T. and Tao,
831 S.: Analysis of transpacific transport of black carbon during HIPPO-3: implications for black
832 carbon aging, Atmospheric Chemistry and Physics, 14(12), 6315–6327, doi:10.5194/acp-14-
833 6315-2014, 2014.

834 Shindell, D., Kuylenstierna, J. C. I., Vignati, E., Dingenen, R. van, Amann, M., Klimont, Z.,
835 Anenberg, S. C., Muller, N., Janssens-Maenhout, G., Raes, F., Schwartz, J., Faluvegi, G., Pozzoli,
836 L., Kupiainen, K., Höglund-Isaksson, L., Emberson, L., Streets, D., Ramanathan, V., Hicks, K.,
837 Oanh, N. T. K., Milly, G., Williams, M., Demkine, V. and Fowler, D.: Simultaneously Mitigating
838 Near-Term Climate Change and Improving Human Health and Food Security, Science,
839 335(6065), 183–189, doi:10.1126/science.1210026, 2012.

840 Solomon, S., Thompson, D. W. J., Portmann, R. W., Oltmans, S. J. and Thompson, A. M.: On the
841 distribution and variability of ozone in the tropical upper troposphere: Implications for tropical
842 deep convection and chemical-dynamical coupling, Geophysical Research Letters, 32(23),
843 doi:10.1029/2005GL024323, 2005.

844 Stauffer, R. M., Thompson, A. M. and Witte, J. C.: Characterizing Global Ozonesonde Profile
845 Variability From Surface to the UT/LS With a Clustering Technique and MERRA-2 Reanalysis,
846 Journal of Geophysical Research: Atmospheres, 123(11), 6213–6229,
847 doi:10.1029/2018JD028465, 2018.

848   Stedman, D. H., Daby, E. E., Stuhl, F. and Niki, H.: Analysis of Ozone and Nitric Oxide by a
849   Chemiluminescent Method in Laboratory and Atmospheric Studies of Photochemical Smog,
850   Journal of the Air Pollution Control Association, 22(4), 260–263,
851   doi:10.1080/00022470.1972.10469635, 1972.

852   Tarasick, D., Galbally, I. E., Cooper, O. R., Schultz, M. G., Ancellet, G., Leblanc, T., Wallington, T.
853   J., Ziemke, J., Liu, X., Steinbacher, M., Staehelin, J., Vigouroux, C., Hannigan, J. W., García, O.,
854   Foret, G., Zanis, P., Weatherhead, E., Petropavlovskikh, I., Worden, H., Osman, M., Liu, J.,
855   Chang, K.-L., Gaudel, A., Lin, M., Granados-Muñoz, M., Thompson, A. M., Oltmans, S. J., Cuesta,
856   J., Dufour, G., Thouret, V., Hassler, B., Trickl, T. and Neu, J. L.: Tropospheric Ozone Assessment
857   Report: Tropospheric ozone from 1877 to 2016, observed levels, trends and uncertainties, Elem
858   Sci Anth, 7(1), 39, doi:10.1525/elementa.376, 2019a.

859   Tarasick, D. W. and Bottenheim, J. W.: Surface ozone depletion episodes in the Arctic and
860   Antarctic from historical ozonesonde records, Atmospheric Chemistry and Physics, 2(3), 197–
861   205, doi:https://doi.org/10.5194/acp-2-197-2002, 2002.

862   Tarasick, D. W., Carey-Smith, T. K., Hocking, W. K., Moeini, O., He, H., Liu, J., Osman, M. K.,
863   Thompson, A. M., Johnson, B. J., Oltmans, S. J. and Merrill, J. T.: Quantifying stratosphere-
864   troposphere transport of ozone using balloon-borne ozonesondes, radar windprofilers and
865   trajectory models, Atmospheric Environment, 198, 496–509,
866   doi:10.1016/j.atmosenv.2018.10.040, 2019b.

867   Thompson, A. M., Johnson, J. E., Torres, A. L., Bates, T. S., Kelly, K. C., Atlas, E., Greenberg, J. P.,
868   Donahue, N. M., Yvon, S. A., Saltzman, E. S., Heikes, B. G., Mosher, B. W., Shashkov, A. A. and
869   Yegorov, V. I.: Ozone observations and a model of marine boundary layer photochemistry
870   during SAGA 3, Journal of Geophysical Research: Atmospheres, 98(D9), 16955–16968,
871   doi:10.1029/93JD00258, 1993.

872   Thompson, A. M., Pickering, K. E., McNamara, D. P., Schoeberl, M. R., Hudson, R. D., Kim, J. H.,
873   Browell, E. V., Kirchhoff, V. W. J. H. and Nganga, D.: Where did tropospheric ozone over
874   southern Africa and the tropical Atlantic come from in October 1992? Insights from TOMS, GTE
875   TRACE A, and SAFARI 1992, Journal of Geophysical Research: Atmospheres, 101(D19), 24251–
876   24278, doi:10.1029/96JD01463, 1996.

877   Thompson, A. M., Doddridge, B. G., Witte, J. C., Hudson, R. D., Luke, W. T., Johnson, J. E.,
878   Johnson, B. J., Oltmans, S. J. and Weller, R.: A tropical Atlantic Paradox: Shipboard and satellite
879   views of a tropospheric ozone maximum and wave-one in January–February 1999, Geophysical
880   Research Letters, 27(20), 3317–3320, doi:10.1029/1999GL011273, 2000.

881   Thompson, A. M., Miller, S. K., Tilmes, S., Kollonige, D. W., Witte, J. C., Oltmans, S. J., Johnson,
882   B. J., Fujiwara, M., Schmidlin, F. J., Coetzee, G. J. R., Komala, N., Maata, M., Mohamad, M. B.,
883   Nguyo, J., Mutai, C., Ogino, S. Y., Silva, F. R. D., Leme, N. M. P., Posny, F., Scheele, R., Selkirk, H.
884   B., Shiotani, M., Stbi, R., Levrat, G., Calpini, B., Thouret, V., Tsuruta, H., Canossa, J. V., Vmel, H.,
885   Yonemura, S., Diaz, J. A., Thanh, N. T. T. and Ha, H. T. T.: Southern Hemisphere Additional

886   Ozonesondes (SHADOZ) ozone climatology (2005-2009): Tropospheric and tropical tropopause
887   layer (TTL) profiles with comparisons to OMI-based ozone products, Journal of Geophysical
888   Research Atmospheres, 117(23), D23301, doi:10.1029/2011JD016911, 2012.

889   Thompson, A. M., Witte, J. C., Sterling, C., Jordan, A., Johnson, B. J., Oltmans, S. J., Fujiwara, M.,
890   Vömel, H., Allaart, M., Piters, A., Coetzee, G. J. R., Posny, F., Corrales, E., Diaz, J. A., Félix, C.,
891   Komala, N., Lai, N., Ahn Nguyen, H. T., Maata, M., Mani, F., Zainal, Z., Ogino, S., Paredes, F.,
892   Penha, T. L. B., da Silva, F. R., Sallons-Mitro, S., Selkirk, H. B., Schmidlin, F. J., Stübi, R. and
893   Thiongo, K.: First Reprocessing of Southern Hemisphere Additional Ozonesondes (SHADOZ)
894   Ozone Profiles (1998-2016): 2. Comparisons With Satellites and Ground-Based Instruments:
895   SHADOZ Data Evaluation, Journal of Geophysical Research: Atmospheres,
896   doi:10.1002/2017JD027406, 2017.

897   Thompson, A. M., Smit, H. G. J., Witte, J. C., Stauffer, R. M., Johnson, B. J., Morris, G., von der
898   Gathen, P., Van Malderen, R., Davies, J., Piters, A., Allaart, M., Posny, F., Kivi, R., Cullis, P., Hoang
899   Anh, N. T., Corrales, E., Machinini, T., da Silva, F. R., Paiman, G., Thiong'o, K., Zainal, Z., Brothers,
900   G. B., Wolff, K. R., Nakano, T., Stübi, R., Romanens, G., Coetzee, G. J. R., Diaz, J. A., Mitro, S.,
901   Mohamad, M. and Ogino, S.-Y.: Ozonesonde Quality Assurance: The JOSIE–SHADOZ (2017)
902   Experience, Bull. Amer. Meteor. Soc., 100(1), 155–171, doi:10.1175/BAMS-D-17-0311.1, 2019.

903   Thompson, C. R., Ryerson, T. B., Peischl, J., Barletta, B., Blake, D. R., Butler, A. H., Crounse, J. D.,
904   Evans, M. J., Fisher, J. A., Huey, L. G., Kim, M. J., Laubach, A., Moore, F. L., Ray, E. A., Murray, L.
905   T., Sherwen, T., Strode, S. A., Wennberg, P. O. and Yu, P.: Global-scale Airborne Observations of
906   Tropospheric Reactive Nitrogen Species from the NASA Atmospheric Tomography Mission, AGU
907   Fall Meeting Abstracts, 14 [online] Available from:
908   http://adsabs.harvard.edu/abs/2017AGUFM.A14D..02T (Accessed 16 March 2020b), 2017.

909   Thouret, V., Marenco, A., Logan, J. A., Nédélec, P. and Grouhel, C.: Comparisons of ozone
910   measurements from the MOZAIC airborne program and the ozone sounding network at eight
911   locations, Journal of Geophysical Research: Atmospheres, 103(D19), 25695–25720,
912   doi:10.1029/98JD02243, 1998.

913   Tilmes, S., Lamarque, J.-F., Emmons, L. K., Conley, A., Schultz, M. G., Saunois, M., Thouret, V.,
914   Thompson, A. M., Oltmans, S. J., Johnson, B. and Tarasick, D.: Technical Note: Ozonesonde
915   climatology between 1995 and 2011: description, evaluation and applications, Atmospheric
916   Chemistry and Physics, 12(16), 7475–7497, doi:https://doi.org/10.5194/acp-12-7475-2012,
917   2012.

918   Trickl, T., Cooper, O. R., Eisele, H., James, P., Mücke, R. and Stohl, A.: Intercontinental transport
919   and its influence on the ozone concentrations over central Europe: Three case studies, Journal
920   of Geophysical Research: Atmospheres, 108(D12), doi:10.1029/2002JD002735, 2003.

921   Williams, J. E., Scheele, M. P., van Velthoven, P. F. J., Thouret, V., Saunois, M., Reeves, C. E. and
922   Cammas, J.-P.: The influence of biomass burning and transport on tropospheric composition
923   over the tropical Atlantic Ocean and Equatorial Africa during the West African monsoon in

924   2006, Atmospheric Chemistry and Physics, 10(20), 9797–9817, doi:10.5194/acp-10-9797-2010,
925   2010.

926   Witte, J. C., Thompson, A. M., Smit, H. G. J., Vömel, H., Posny, F. and Stübi, R.: First
927   Reprocessing of Southern Hemisphere ADditional OZonesondes Profile Records: 3. Uncertainty
928   in Ozone Profile and Total Column, Journal of Geophysical Research: Atmospheres, 123(6),
929   3243–3268, doi:10.1002/2017JD027791, 2018.

930   Wofsy, S. C.: HIAPER Pole-to-Pole Observations (HIPPO): fine-grained, global-scale
931   measurements of climatically important atmospheric gases and aerosols, Philosophical
932   Transactions of the Royal Society A: Mathematical, Physical and Engineering Sciences,
933   369(1943), 2073–2086, doi:10.1098/rsta.2010.0313, 2011.

934   Young, P. J., Archibald, A. T., Bowman, K. W., Lamarque, J.-F., Naik, V., Stevenson, D. S., Tilmes,
935   S., Voulgarakis, A., Wild, O., Bergmann, D., Cameron-Smith, P., Cionni, I., Collins, W. J., Dalsøren,
936   S. B., Doherty, R. M., Eyring, V., Faluvegi, G., Horowitz, L. W., Josse, B., Lee, Y. H., MacKenzie, I.
937   A., Nagashima, T., Plummer, D. A., Righi, M., Rumbold, S. T., Skeie, R. B., Shindell, D. T., Strode,
938   S. A., Sudo, K., Szopa, S. and Zeng, G.: Pre-industrial to end 21st century projections of
939   tropospheric ozone from the Atmospheric Chemistry and Climate Model Intercomparison
940   Project (ACCMIP), Atmos. Chem. Phys., 13(4), 2063–2090, doi:10.5194/acp-13-2063-2013,
941   2013.

942   Zhang, B., Owen, R. C., Perlinger, J. A., Helmig, D., Martín, M. V., Kramer, L., Mazzoleni, L. R. and
943   Mazzoleni, C.: Ten-year chemical signatures associated with long-range transport observed in
944   the free troposphere over the central North Atlantic, Elem Sci Anth, 5(0),
945   doi:10.1525/elementa.194, 2017.

946   Zhang, L., Jacob, D. J., Boersma, K. F., Jaffe, D. A., Olson, J. R., Bowman, K. W., Worden, J. R.,
947   Thompson, A. M., Avery, M. A., Cohen, R. C., Dibb, J. E., Flock, F. M., Fuelberg, H. E., Huey, L. G.,
948   McMillan, W. W., Singh, H. B. and Weinheimer, A. J.: Transpacific transport of ozone pollution
949   and the effect of recent Asian emission increases on air quality in North America: an integrated
950   analysis using satellite, aircraft, ozonesonde, and surface observations, Atmospheric Chemistry
951   and Physics, 8(20), 6117–6136, doi:https://doi.org/10.5194/acp-8-6117-2008, 2008.

952

953
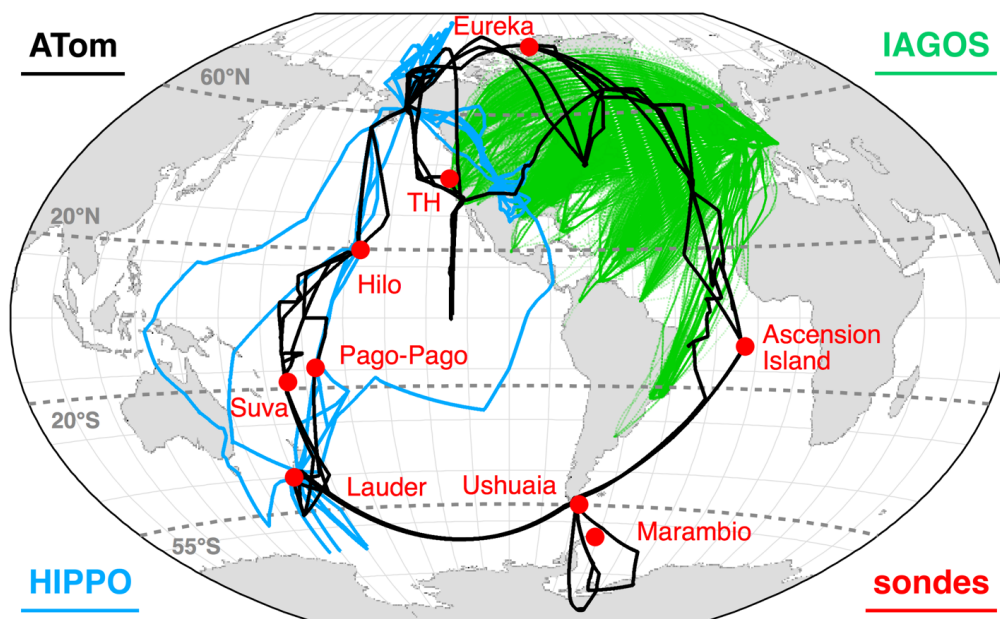
Figure 1 The location and flight tracks of all O$_3$ monitoring platforms used in this work are illustrated with different markers and colors. The ATom flight track is in black, the HIPPO flight track is in blue, IAGOS flight paths are in green, and the ozonesonde launching sites are indicated by the red markers. The dotted grey lines define the latitudinal bands over which individual ATom and HIPPO profiles were averaged to derive a regional O$_3$ distribution: the tropics (20° S – 20° N), the midlatitudes (55° S – 20° S; 20° N – 60° N), and the high-latitudes (90° S – 55° S; 60° N – 90° N). Only data from remote oceanic flight segments of ATom and HIPPO missions were used in this work.
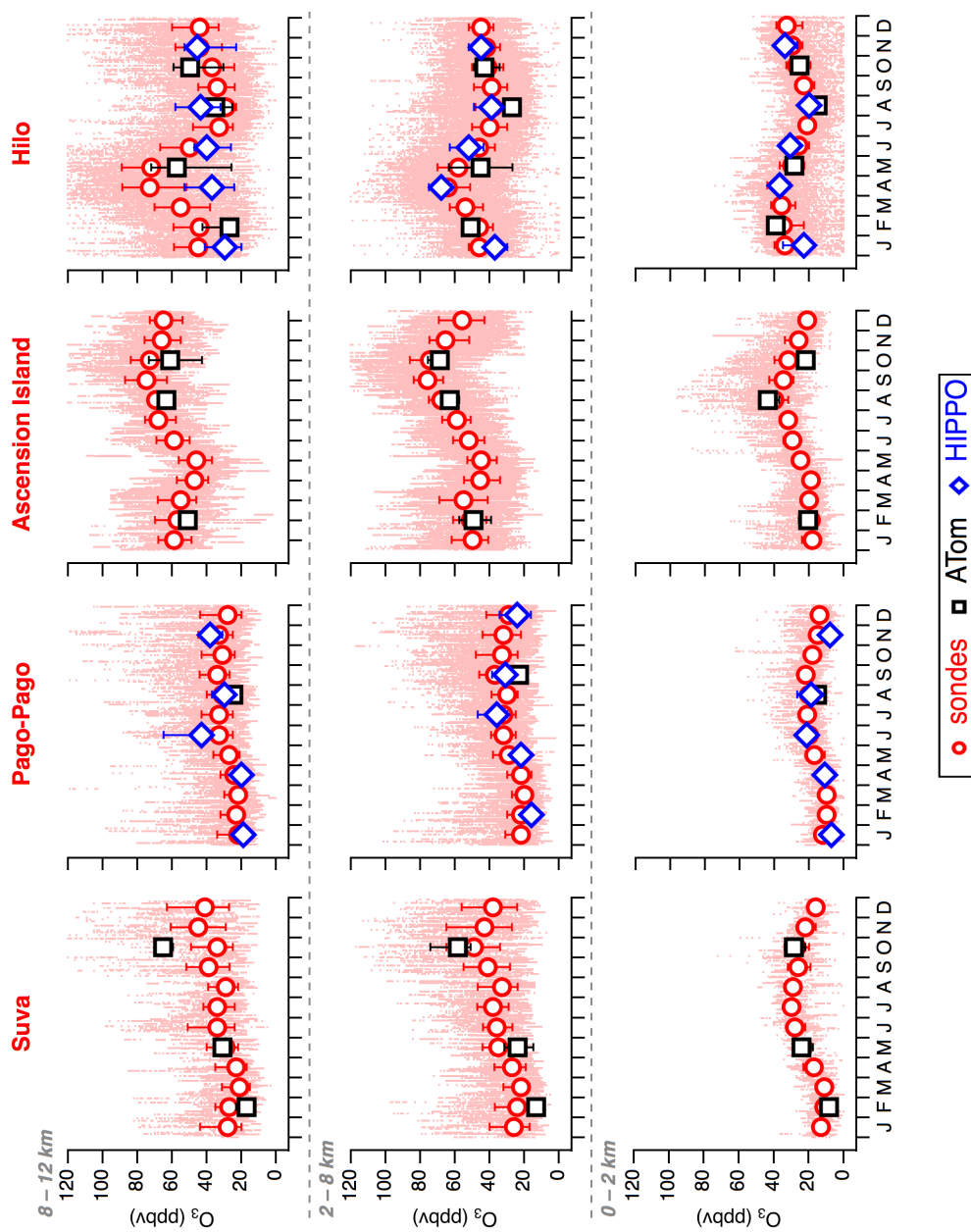
Figure 2 Comparison of ATom (black squares) and HIPPO (blue diamonds) monthly median O_3 with ozonesonde (red circles) records from the four tropical sites. Markers indicate the median and the bars indicate the 25th and 75th percentiles. The three rows, from bottom to top, correspond to the boundary layer (0–2 km), the free troposphere (2–8 km), and the UTLS (8–12 km). The pink dots show every O_3 data point measured by ozonesondes for the timeframes indicated in Table S2.
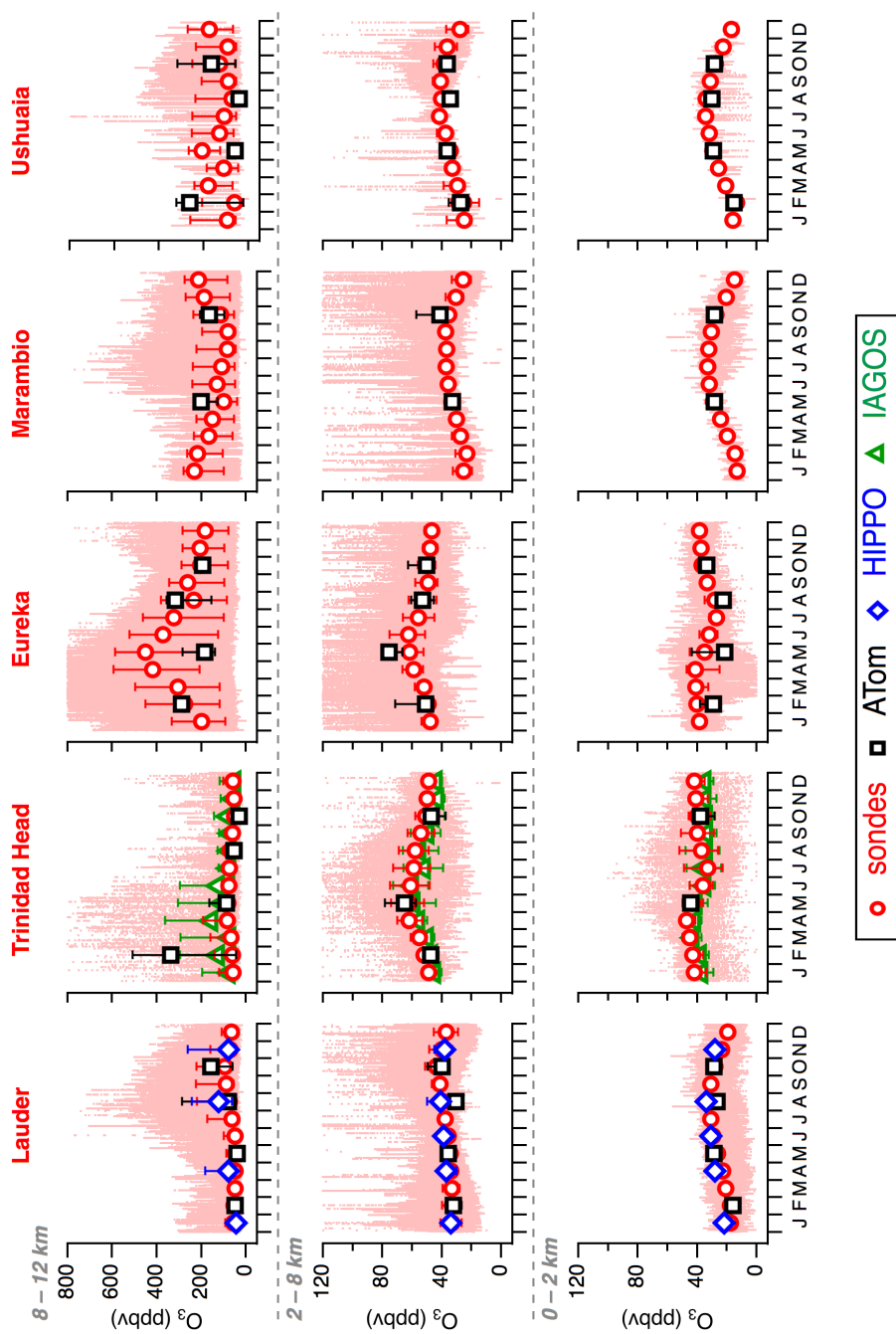
Figure 3 Same as in Figure 2 but for ozonesonde launching sites located in the middle- and high-latitudes. O_3 data obtained from the IAGOS program (green triangles) during descents into San Francisco Bay-area airports were also added to the Trinidad Head site for comparison.
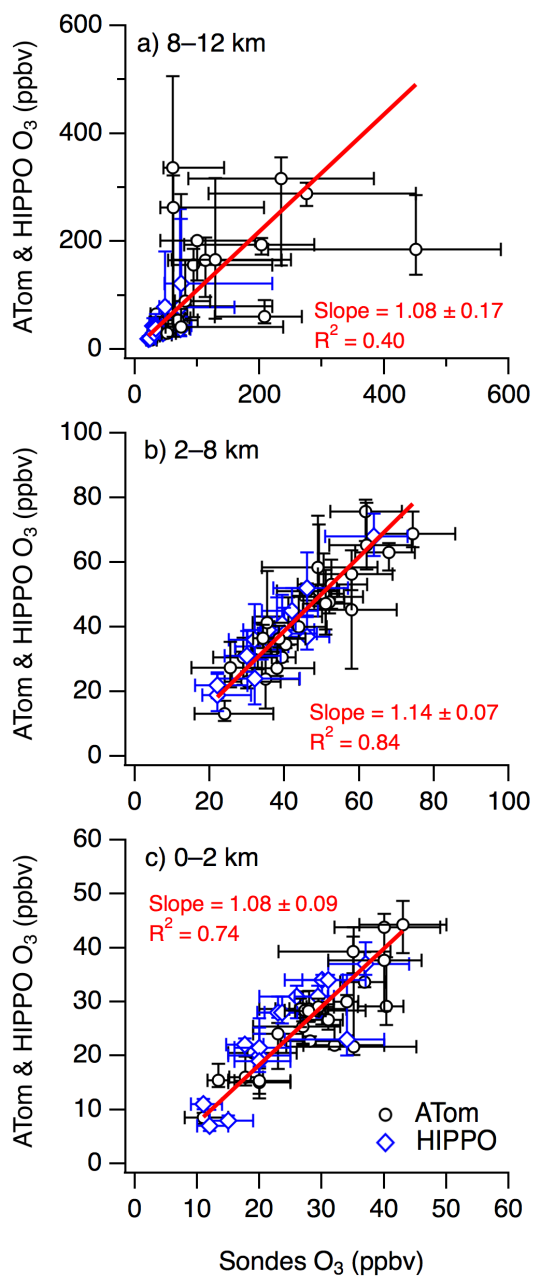
Figure 4 ATom (black circles) and HIPPO (blue diamonds) combined monthly median O_3 vs. monthly median O_3 from ozonesondes at the nine sites considered in this study. The three panels

indicate the correlations for a) the UTLS (8–12 km), b) the free troposphere (2–8 km), and c) the boundary layer (0–2 km). The orthogonal regression fits are two-sided but not weighted.
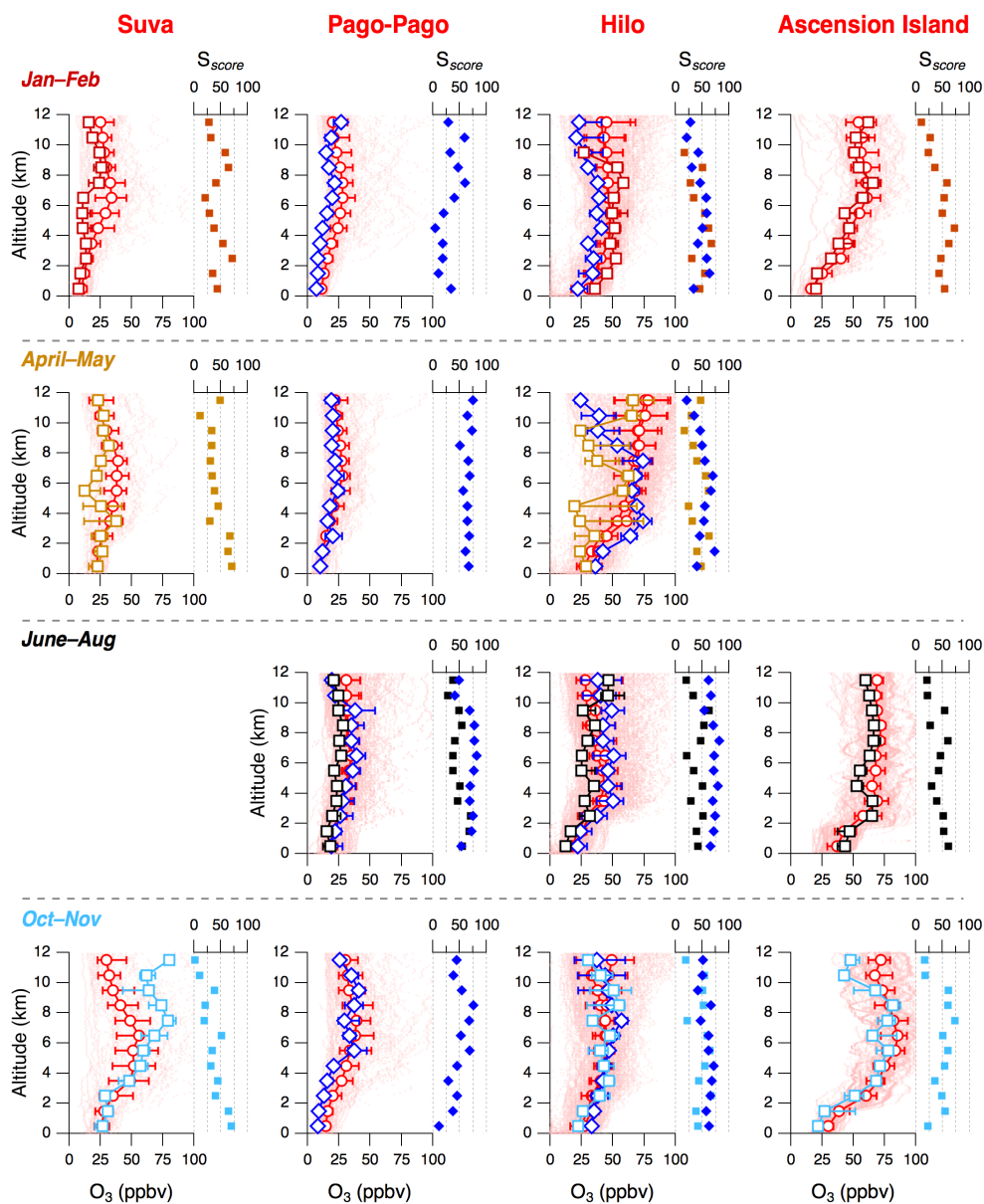
Figure 5 Seasonal comparison of 1 km-vertically-binned ATom (colored squares) and HIPPO (blue diamonds) median O_3 with ozonesonde (red circles) records at four sites in the tropics (Suva in Fiji, Pago-Pago in American Samoa, Hilo in Hawaii, and Ascension Island). Markers indicate the median and the bars are the 25th and 75th percentiles. The S_{score} is a metric of how well ATom

and HIPPO 1 km-binned O_3 probability distribution functions (PDFs) overlap with the corresponding 1 km-binned O_3 PDFs from ozonesondes. The S_{score} shown with squares compares ATom with ozonesondes, and the S_{score} shown with blue diamonds compares HIPPO with ozonesondes. The pink dots show every O_3 data point measured by ozonesondes for the timeframes indicated in Table S2.
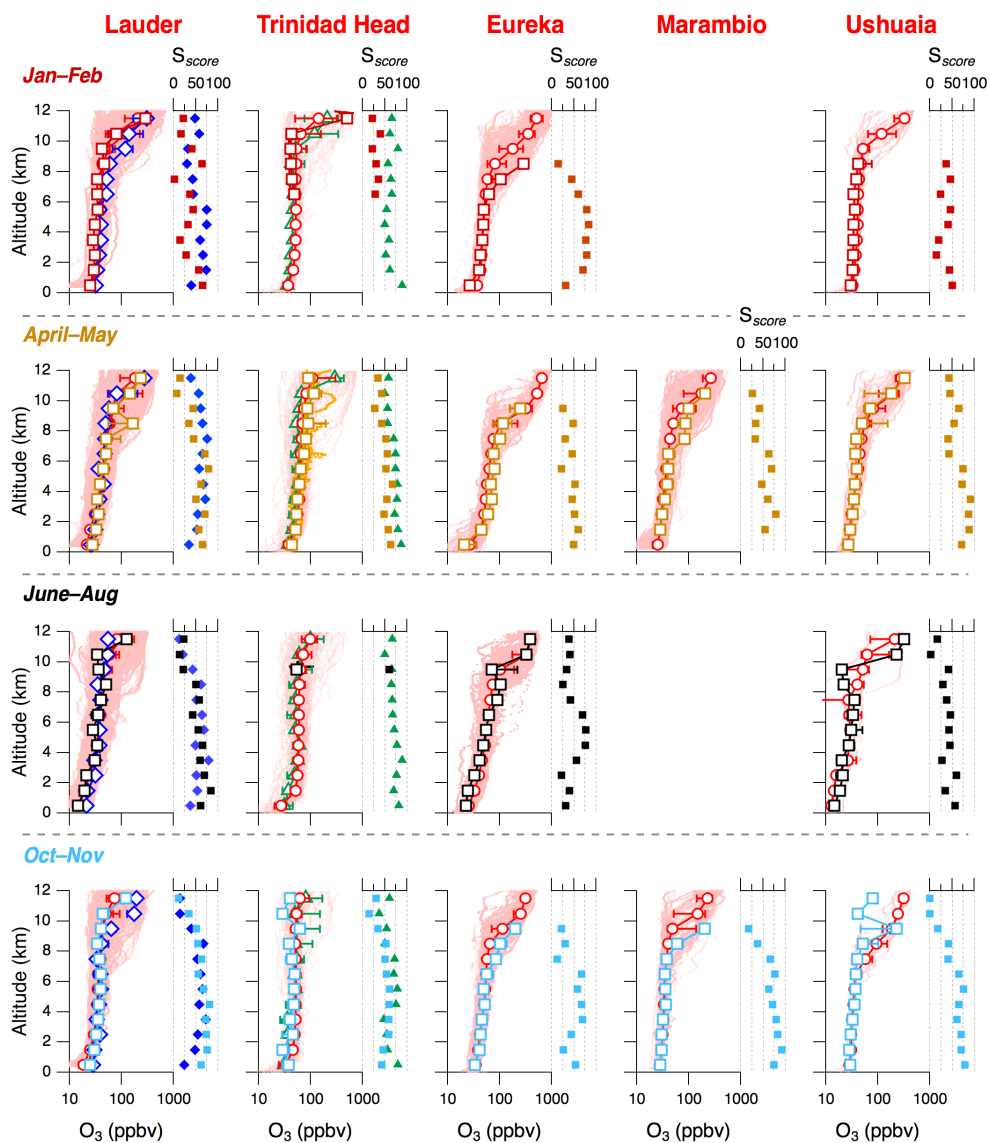
Figure 6 Same as in Figure 5 but for ozonesonde launching sites located in middle- and high-latitudes (Lauder in New Zealand, Trinidad Head in the USA, Eureka in Canada, Ushuaia in Argentina, and Marambio in Antarctica). O_3 data obtained from the IAGOS program (green triangles) during descents into San Francisco Bay-area nearby airports were also added to the Trinidad Head site for comparison.
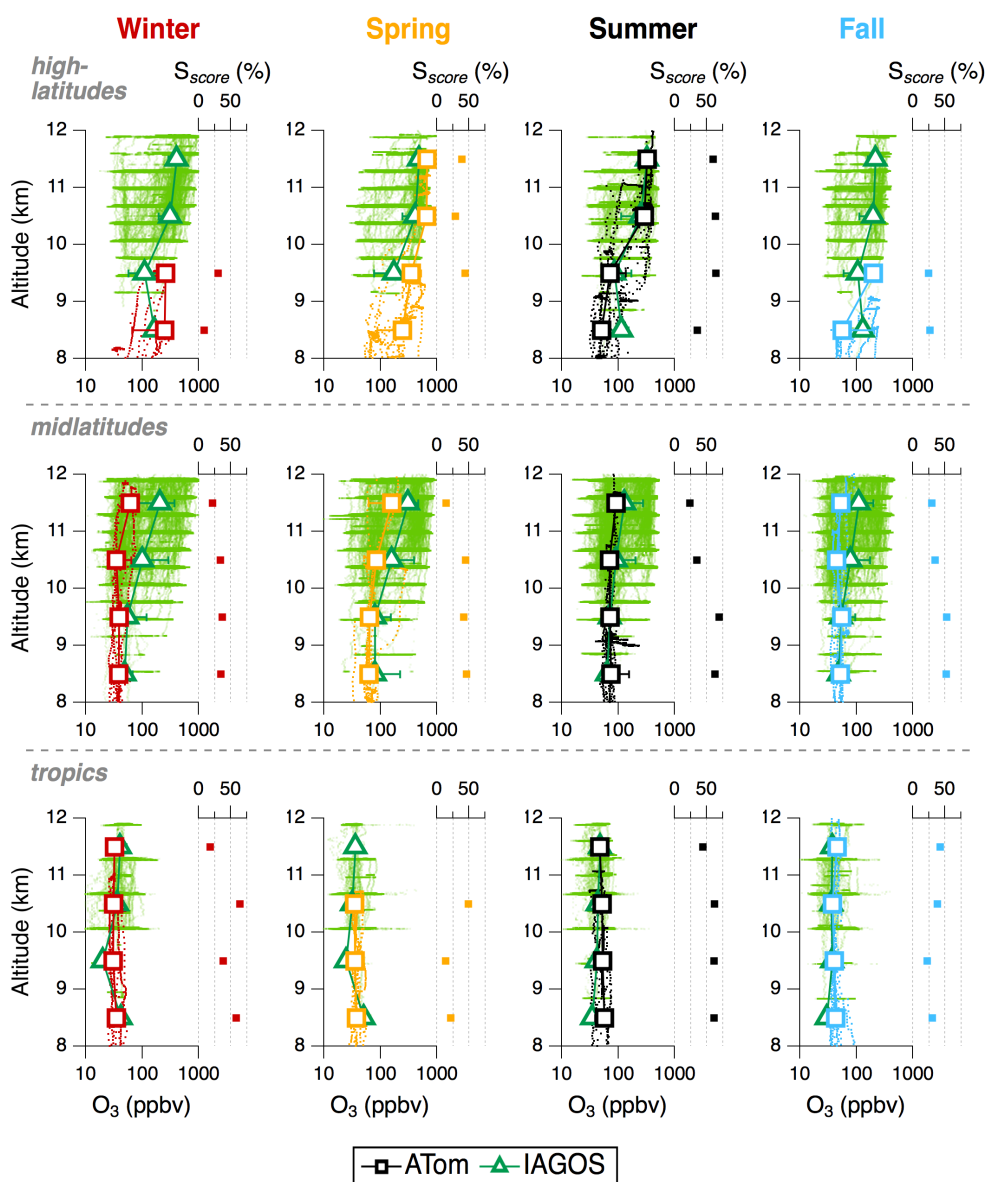
Figure 7 Seasonal comparison of 1 km-binned ATom (colored squares) median O₃ with IAGOS (green triangles) in the northern Atlantic UTLS. Markers indicate the median and the bars are the 25th and 75th percentiles. The three different rows indicate the latitudinal bands. The four columns

indicate the seasons. The green dots show every O₃ data point measured by IAGOS flights for the timeframe indicated in Table S1.
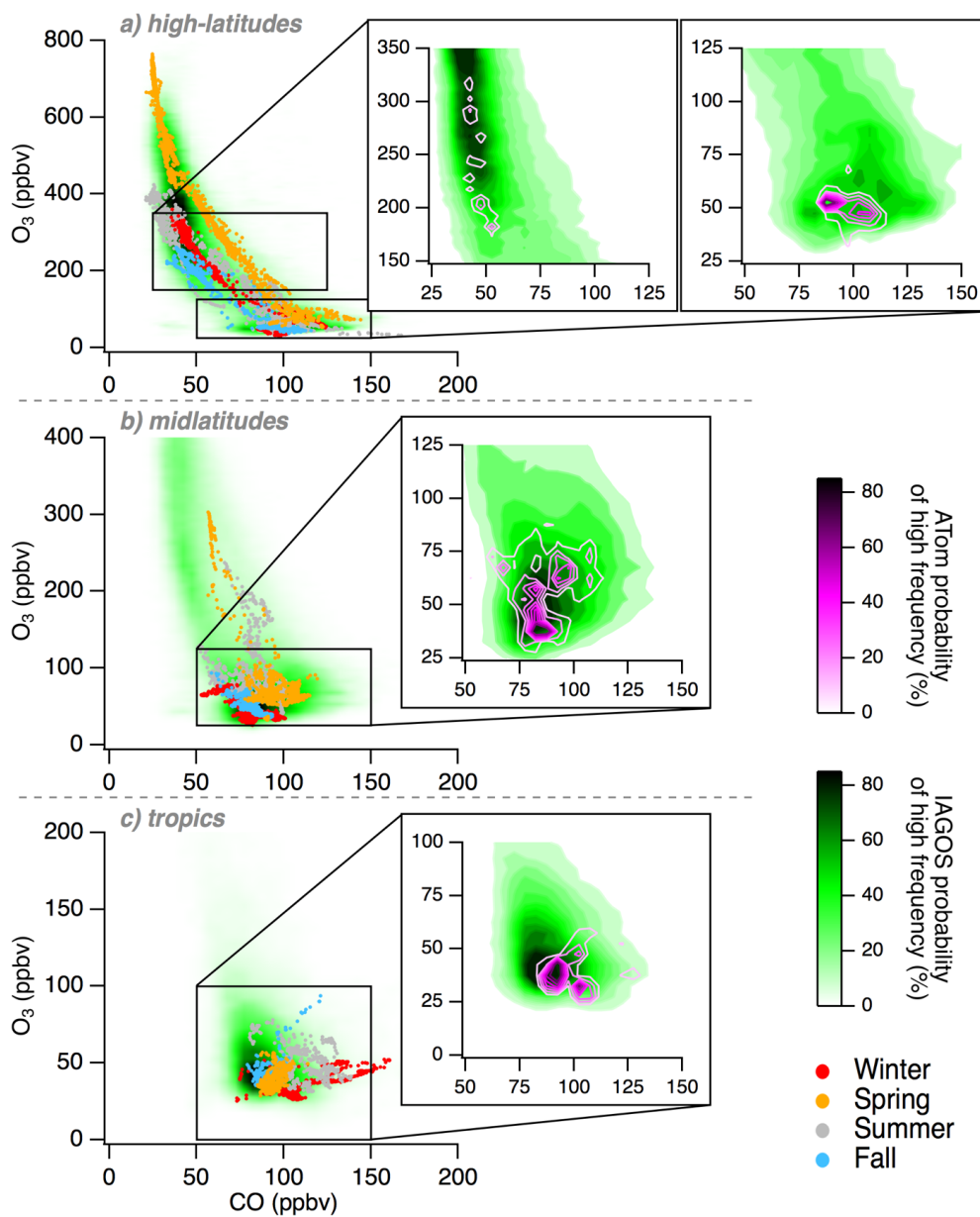
Figure 8 IAGOS and ATom seasonal O₃ vs. CO scatterplots, with insets showing the most frequent O₃ values measured during IAGOS and ATom. ATom seasonal deployments are

colored according to the legend. The frequency gradient of O_3 counts is illustrated by the color scales (green for IAGOS, magenta for ATom). ATom measurements have been combined for the frequency gradients shown in the insets. The probability of high frequency refers to the probability of finding frequently measured O_3 values within the contour boundaries
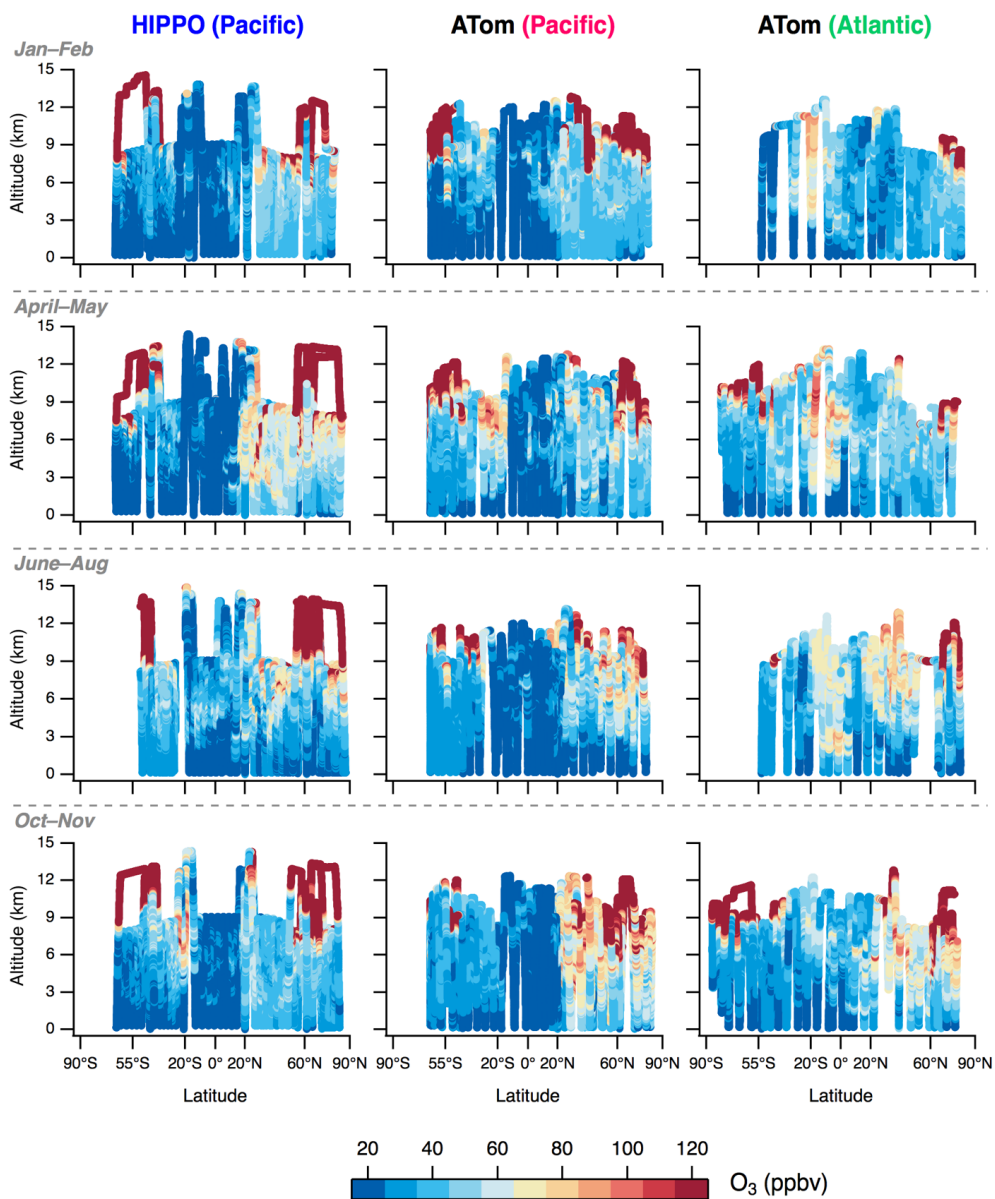
Figure 9 Global-scale distribution of tropospheric O_3 for each ATom and HIPPO seasonal deployment. The rows separate the seasonal deployments, while the columns indicate the mission and the ocean basin. The O_3 color-scale ranges from 20 to 120 ppbv, and all values outside of this

range are shown with the same extremum color (red for values > 120 ppbv, blue for values < 20 ppbv). HIPPO deployments in June and August were combined together.
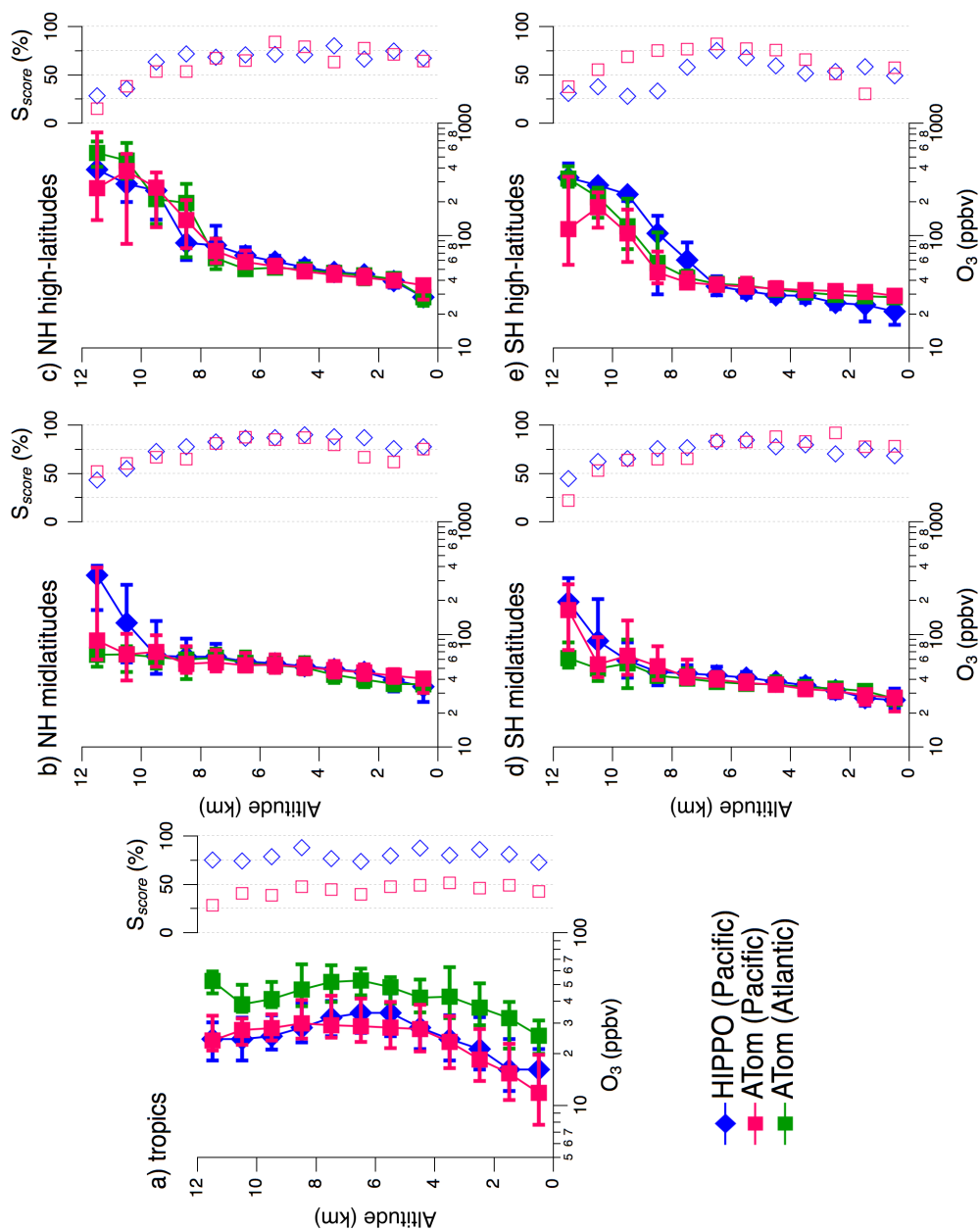
Figure 10 Vertically-resolved O_3 distributions from 0–12 km are plotted for the Atlantic (ATom in green) and for the Pacific (ATom in pink, HIPPO in blue). The five broad latitude regions correspond to the data parsing illustrated by Fig. 1. Markers indicate median O_3, and bars are the

25th and 75th percentiles, per 1 km altitude bin. Note the log scale on the x-axis. S_{score} values resulting from the comparison of HIPPO and ATom Pacific distributions are shown with blue diamonds, and from the comparison of ATom Atlantic and Pacific distributions with pink squares.
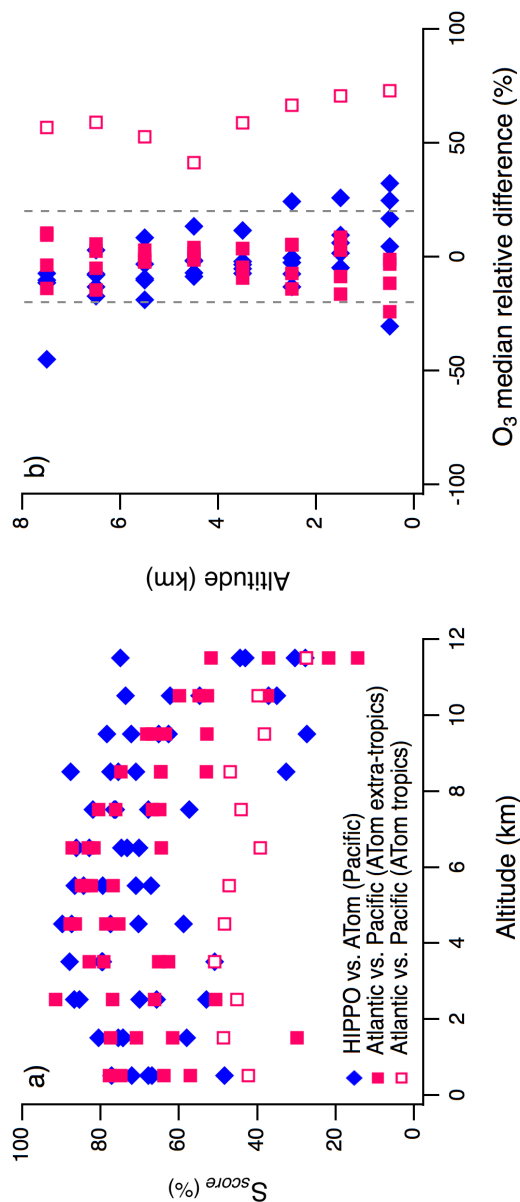
Figure 11 All S$_{score}$ values from Fig. 10 are shown in panel a) and plotted against altitude. The
HIPPO and ATom comparison in the Pacific basin is shown with blue diamonds, and a comparison
of the Atlantic and Pacific basins during ATom is shown with filled pink squares for the extra-

tropics and open pink squares for the tropics. The relative difference of median O_3 from 0 to 8 km given in Fig. 10 is shown in panel b), with the same color and marker code as in panel a). The dotted grey lines indicate a relative difference of 20 %.
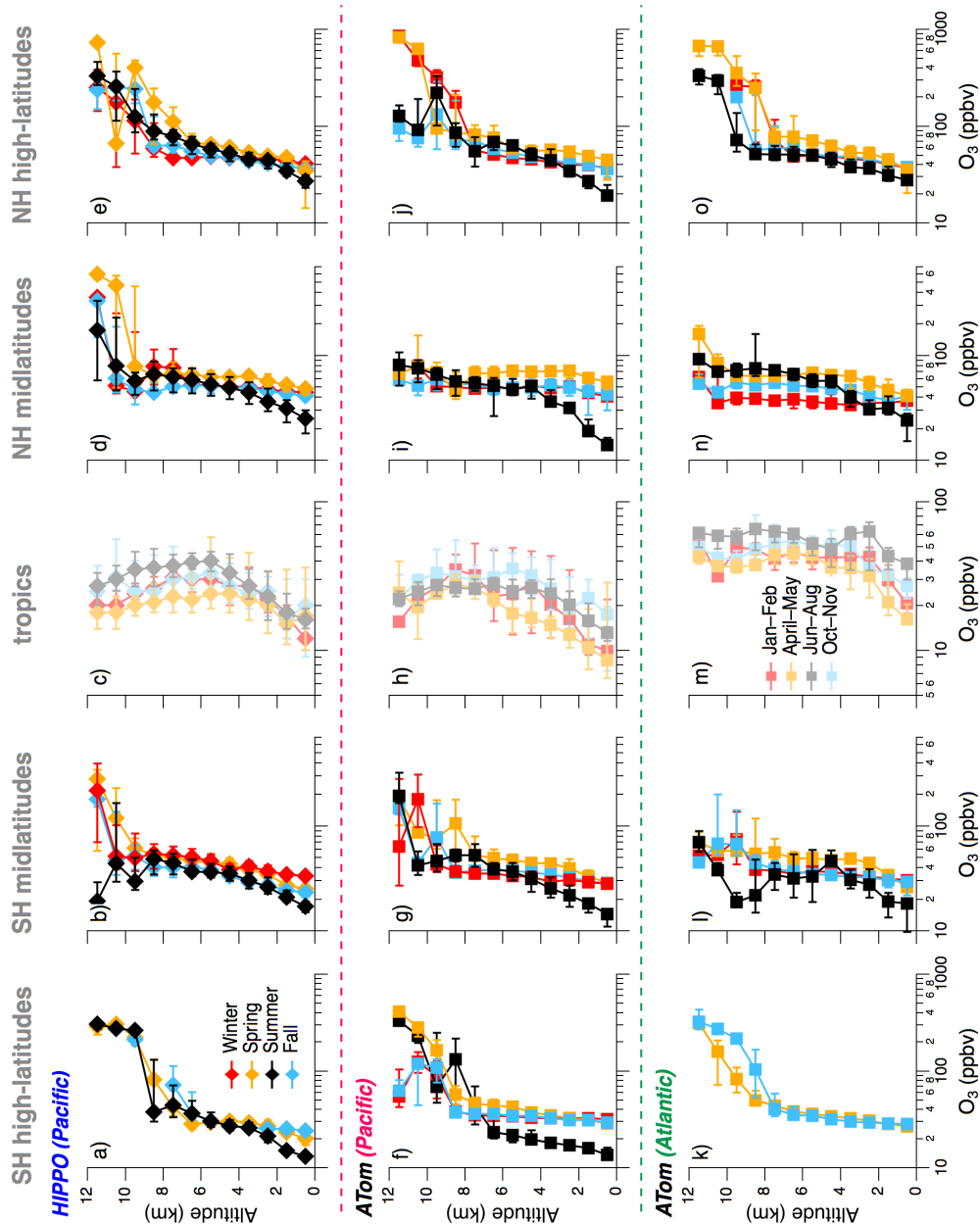
Figure 12 Seasonal variability of regional O₃ distribution in the Pacific (HIPPO in the first and
ATom in the second row) and in the Atlantic (ATom in the third row). The colors designate the

local seasons with red as winter, gold as spring, black as summer, and blue as fall (corresponding months are indicated for the tropics, with lighter colors). The markers and associated bars correspond to the median, 25th and 75th percentiles, respectively, of O_3 distribution in every 1 km altitude bin. Note the logarithmic scale on the x-axes in all panels, and the changing scale with latitudinal bin.

Figure 13 O₃ vs. CO plots using combined ATom and HIPPO data. Each panel denotes a different latitudinal band in each basin. Seasonal deployments are colored according to the legend. Note the logarithmic scale on the y-axes in all panels, and the changing scale with latitudinal bin